Masterarbeit

Retinotopic Mapping

Ausgeführt am Institut für
medizinische Physik und biomedizinsche Technik
der Medizinischen Universität Wien

unter der Anleitung von
Univ.-Prof. Dr. Gerald Badurek
Assoc.-Prof. Priv.-Doz. Dr. Christian Windischberger
durch

Allan Hummer, B.Sc.
Oeverseestraße 25-29/4/4
1150 Wien

Wien, 16.07.2013

Contents

Kurzfassung

Während der zweiten Hälfte des 20. Jahrhunderts entwickelte sich die Magnetresonanztomographie (MRT) zu einem der wichtigsten Werkzeuge der klinischen Diagnostik und wird nun in Krankenhäusern weltweit routinemäßig angewandt. Die Entdeckung des "blood oxygen level dependent" (BOLD) Kontrastes in den 1990ern ermöglichte neben anatomischen Untersuchungen unseres kompliziertesten Organes, des Gehirns, auch funktionelle Analysen während der Ausführung bestimmter Aufgaben.

Der Okzipitallappen, im Speziellen der visuelle Kortex, stellt das Hauptziel visueller Signale und damit das visuelle Verarbeitungszentrum dar. Jedoch wird nicht der ganze visuelle Kortex benötigt um ein bestimmtes visuelles Signal zu verarbeiten. Die Regionen im primären visuellen Kortex sind für die Verarbeitung bestimmter visueller Signale verantwortlich basierend auf der Gesichtsfeldhälfte, der Art der Ganglienzelle und der Position der Ganglienzelle in der Retina in der das Signal seinen Ursprung hat. Auf dieser sogenannten "Retinotopie", welche die Beziehung zwischen der räumlichen Ganglienzellenposition in der Retina und der Lage der entsprechenden Neuronen im visuellen Kortex beschreibt, liegt der Fokus dieser Masterarbeit.

Für jedes Voxel im visuellen Kortex gibt es eine entsprechende Region im Gesichtsfeld. Umgekehrt wird jeder Ort im Gesichtsfeld auf eine bestimmte Region im visuellen Kortex abgebildet. Dies kann grafisch als "retinotopische Karte" dargestellt werden.

Um eine solche Karte zu erhalten wurde eine "traveling wave" Analyse basierend auf rotierenden Keil und sich vergrößernden Ring Stimuli aufgesetzt. Diese periodischen Stimuli wurden durch zwei sinusförmige Regressoren modeliert. Nachdem die Methode mittels künstlich erzeugter Daten überprüft wurde, wurde sie auf gemessene Daten angewandt. Durch Überlagerung auf eine

abgeflachte Darstellung der grauen Substanz konnten die Erbnisse visualisiert werden. Die Retinotopie kann auf dieser Oberfläche durch benachbarte Halbkreise für den vergrößernden Ring Stimulus und durch Keile für den rotierenden Keil Stimulus beobachtet werden. Mit der Hilfe beider Stimuli kann also ein beliebiger Punkt des Gesichtsfeldes durch Polarkoordinaten beschrieben werden.

Um genauere retinotopische Karten zu schaffen wurden zusätzliche Messungen vorgenommen und mit Hilfe einer erst kürzlich vorgestellten Methode namens "population receptive field (pRF) mapping" ausgewertet [1]. Die funktionellen Daten wurden mittels einer sogenannten "multiband EPI" Sequenz aufgenommen, die durch die gleichzeitige Anregung mehrerer Schichten verglichen mit Standardsequenzen weitaus höhere Auflösungen ermöglichte. Neben den regulären Stimuli wurden auch zentrale und periphere Gesichtsfeldausfälle simuliert. Die pRF Analyse zeigte, dass der okzipitale Pol auf visuelle Stimuli welche im Gesichtsfeldzentrum präsentiert werden reagiert. Regionen welche sich anterior davon befinden reagieren hingegen auf periphere Stimuli. Bei den simulierten lokalen Gesichtsfeldausfällen wurde genau bei jenen Voxeln keine funktionelle Aktivierung festgestellt, welche zuvor durch eine reguläre Stimulation eben diesen Gesichtsfeldregionen zugeordnet wurden.

Die Erzeugung von exakten retinotopischen Karten könnte zum besseren Verständnis von Krankheiten dienen, welche fokale Gesichtsfeldausfällen verursachen. Beispiele dafür sind die altersbedinge Makuladegeneration und das Glaukom, auch grüner Star genannt.

Abstract

In the second half of the 20th century magnetic resonance imaging (MRI) evolved to one of the most important tools in clinical diagnostics and is now used in hospitals around the world as an indispensable tool on a daily basis. The discovery of the "blood oxygen level dependent" (BOLD) contrast in the 1990s made it possible to not only analyze the structure of our most complex organ, the brain, but also its function during given tasks.

One of the regions best examined by functional MRI (fMRI) is the occipital lobe, in particular the visual cortex, which is the main target for visual signals and the center of visual processing. Not all of the visual cortex is engaged with processing every visual signal. The regions of the primary visual cortex are responsible for processing visual signals depending on factors like visual hemifield, class of ganglion cell and spatial position of the ganglion cell within the retina. The so-called "retinotopic organization", which describes the relation between the ganglion cells spatial position in the retina and the location of corresponding neurons in the visual cortex is the main focus of this master thesis.

For each voxel in the visual cortex there is a corresponding region of the visual field. On the other hand every location in visual space is mapped onto a specific location of the visual cortex. This results in a "retinotopic map".

To produce such a map a traveling wave analysis approach using rotating wedge and expanding ring stimuli was applied. This periodic stimuli were then estimated with two sinusoidal regressors. After validating the method using artificial data, it was applied on real data. The results are visualized using a flattened gray matter surface. The retinotopy of the visual cortex can be seen in the form of adjacent semicircles for the expanding ring stimulus and wedges for the rotating wedge stimulus on this surfaces. With the help

of both stimuli we can therefore assign an arbitrary visual field region using polar coordinates.

In order to perform more accurate retinotopic mapping additional data has been recorded and evaluated using a recently proposed method for "population receptive field (pRF) mapping" [1]. Functional data was obtained using a "multiband EPI" sequence, which employs simultaneous excitation of several slices to enable higher resolution when compared to conventional sequences. Simulated localized central and peripheral vision loss were also part of this experiment. The pRF analysis showed that the occipital pole corresponds to visual stimuli presented at the center of the visual field, while anterior regions correspond to stimulation of more peripheral regions. Additionally, localized vision loss indeed causes a loss of activation in the voxels which were associated with the affected visual field locations by the full stimulation experiment.

Accurate pRF mapping which is achieved using this technique could be of particular importance for gaining a better understanding for diseases which result in localized loss of vision. Examples are age-related macular degeneration (AMD) and glaucoma.

1. Introduction

Magnetic Resonance Imaging (MRI) represents a one-of-a-kind method to investigate the living organism, in particular the living brain. It provides high resolution and contrary to methods like Computed Tomography (CT), it features excellent soft tissue contrast and does not require ionizing radiation to do so.

The origins of MRI are not long past as Paul Lauterbur and Peter Mansfield described methods to create the first MR images in 1973. In the following years, Mansfield developed faster image acquisition techniques. These attempts culminated in a technique called Echo Planar Imaging (EPI), which he introduced in 1977. EPI yields decreased image quality compared to standard imaging methods, but in return provides us with three-dimensional images taken in a matter of seconds instead of minutes.

This forms the basis for functional Magnetic Resonance Imaging (fMRI). In order to perform fMRI and observe functional changes in measured volume, in our case the human brain, a complete brain image is acquired every few seconds. Investigating the differences of these volumes, we can identify changes in the brain over a period of time.

But how do we know, that it is possible to associate changes of the MR signal in a certain region with brain activity, i.e. firing neurons? Positron emission tomography for example uses radioactive tracers, e.g. Fluorodeoxyglucose, which are transported to regions in need of energy to mark metabolic activity. FMRI on the other hand can succeed without the use of radiating tracers, by using the so called Blood-Oxygen-Level-Dependent (BOLD) contrast first described by Seiji Ogawa in 1990. Ogawa found that blood with oxygen bound to its hemoglobin molecule yields more MR signal then so called deoxygenated blood. Because active brain regions are supplied with arterial, oxygenated,

blood it is possible to identify those areas over a course of time and relate them to performed actions or experienced stimuli of the measured individual.

Visual stimuli, like flickering lights, are typical stimuli, which can be used to elucidate BOLD activation in the occipital lobe, particularly in the visual cortex. The achieved activation maps are not always the same, but related to the type of presented visual stimulus. For example, it is known that presenting a central visual stimulus yields different BOLD activation maps, compared to presenting a peripheral stimulus.

The main topic of this master thesis is to examine the relation of stimulus position in the visual field and corresponding activity in the primary visual cortex. Additionally, simulated localized vision loss, which is achieved by the absence of visual stimuli in certain regions is investigated. This is of great interest, because these localized deficits are also present in diseases like age-related macular degeneration (AMD).

The first part deals with basics of MRI and the human visual system. It also recapitulates previous studies which already engaged retinotopic mapping using fMRI.

Chapter 2 provides a brief overview of the history of MRI. After dealing with the inventions which finally lead to fMRI, the physical basics of Nuclear Magnetic Resonance (NMR) and fMRI are discussed. The concept of spins is introduced and an outline of the imaging process, starting from exploiting magnetic resonance of protons in the body and receiving a signal and closing with image reconstruction, is given.

The human visual system, leading from the eye to the primary visual cortex, is subject of Chapter 3. Among other things, it focuses on the different visual streams and the reorganization of visual information which takes place with respect to different criteria like visual hemifields.

Chapter 4 addresses studies which already dealt with the retinotopic behavior of the visual cortex. It gives a short summary and explains the used stimuli and analysis methods.

The second part of this master thesis focuses on the results obtained during various experiments, which were conducted during this work.

Chapter 5 deals with a traveling wave analysis of retinotopic data sets ob-

tained using the rotating wedge and expanding ring stimulus. The first section is about validating the introduced method written in MATLAB (The MathWorks, Inc., Natick, MA) by using artificial data. In the second section the method is then applied on real data. The chapter is also concerned with the challenge of segmenting the brain in order to produce a flat gray matter surface, which can be used to illustrate the activation patterns calculated.

In Chapter 6, another approach is used to create retinotopic maps. The mrVista toolbox (Wandell lab, Stanford, CA) was used to create non-periodic eight-bar stimuli as well as to analyze the data using population receptive field (pRF) modeling. This, in combination with multiband imaging, allowed for a precise mapping of the primary visual cortex (V1).

Chapter 7 provides conclusions and provides an outlook for future research which could be conducted on this subject.

Part I.

Basic Principles

2. Introduction to Magnetic Resonance Imaging

Findings in physics in the early 20th century influenced almost every field in science. Medicine benefited in particular as it was possible to develop several techniques for non-invasive imaging including positron emission tomography (PET) and magnetic resonance imaging (MRI). MRI evolved to one of the most important tools in clinical diagnostics and is now used in hospitals around the world as an indispensable tool on a daily basis. The discovery of the blood oxygen level dependent (BOLD) contrast in the 1990s made it possible to not only analyze the structure of the most complex organ, our brain, but also its function during given tasks.

2.1. History of magnetic resonance imaging (MRI)

In 1924 Wolfgang Pauli (1900-1958) suggested a new quantum number which was later referred to as the spin of a particle. Isidor Rabi (1898-1988) successfully designed an experiment ("molecular-beam magnetic resonance detection method") which made it possible to confirm Pauli's theory 14 years later [2]. A gaseous beam of nuclei was sent past a magnet and deflected before hitting the detector. Rabi added an electromagnetic magnet which was able to change its field strength rapidly. If a particular combination of field strength and oscillation frequency of the electromagnetic magnet was applied to the beam, it would be deflected differently. Because the values of field strength and resonant oscillation frequency vary for each element Rabi made it pos-

sible to determine the "gyromagnetic ratio" of every element. Furthermore he had proven the existence of nuclear spins and the physical basis of MR started to evolve. After the end of the Second World War both Edward Purcell (1912-1997) and Felix Bloch (1905-1983) independently discovered that the MR-effect which Rabi had discovered in gases can also be observed in solid materials [3,4]. Bloch filed a patent for the first NMR spectrometer in 1946 [5] and shortly thereafter sequences to identify the characteristic rates of signal decay of elements situated in different surroundings were developed [6,7]. Another milestone was the discovery of so called "spin echoes" 1950 by Erwin Hahn (*1921) [8].

Raymond Damadian (*1936) analyzed the T_1 and T_2 relaxation times on various tumors in 1970. He discovered an increase of T_2 when measuring tumors in comparison with healthy tissue [9].

Like Damadian, Paul C. Lauterbur (1929-2007) was a professor at the State University of New York (SUNY), but contrary to Lauterbur he was a physicist and not a physician. Lauterbur thought of a way to perform NMR on living creatures and came up with the idea of magnetic field gradients, which allowed him to study a particular voxel (the three dimensional counterpart to a pixel) inside an organism with a characteristic resonance frequency [10].

Four years later, in 1975, Richard Ernst (*1933) developed a method to simultaneously collect data from a group of voxels by gathering a whole frequency spectra and then applying a Fourier transform in order to extract different frequency components and assigning them to their spatial position [11].

In 1980 Bill Edelstein(1944*) was the primary inventor of "spin-warp" imaging, which was another improvement to Lauterburs paradigm [12]. He proposed a pulsed gradient that could be applied and would result in a positional encoding ("spin warp") which is more efficient than Ernst's approach.

Peter Mansfield (1933*) also played a very important part in the development of MRI. In 1977 he suggested to use rapidly switching gradients to acquire an image in a fraction of the time needed by other methods. This approach, which made it possible to image an entire slice in 100 milliseconds (instead of tens of seconds) is referred to as "Echo Planar Imaging" (EPI).

2.1.1. History of blood oxygen dependent functional MRI (BOLD-fMRI)

Louis Sokoloff (*1921), an American physicist, used radiolabeled (^{14}C) deoxyglucose to determine the intensity of metabolism in various regions of the brain [13]. The higher the energy consumption the more glucose would be drawn in this specific region. After sectioning the animal's brain the activated brain regions were strongly labeled by the radioactive tracer. Sokoloff proceeded to experiment with Fluorodeoxyglucose (18F-FDG) (a positron emitter) and early PET scanners and made it possible to observe metabolism changes in the human living brain [14].

The downside of this and similar techniques is the dependence on radioactive tracers, which may be used to analyze growing tumors but don't seem appropriate for routine examinations. The Japanese researcher Seiji Ogawa (1934*) discovered that the different signals of oxygenated and deoxygenated blood can be used to reveal brain activity in rat brains, establishing BOLD (blood oxygen level dependent) imaging [15].

2.2. Basics of nuclear magnetic resonance (NMR) and magnetic resonance imaging (MRI)

Electrons and nuclei possess so called intrinsic magnetism. This magnetism is a property of the particle, just like spin angular momentum or mass. Magnetism, more precisely the magnetic moment μ, is strongly linked to spin by the gyromagnetic ratio γ. The gyromagnetic ratio is a characteristic factor of a particle/system. It is the ratio of its magnetic dipole moment to its angular momentum (spin), which means that the influence of a magnetic field on a specific particle depends on the gyromagnetic ratio of this particle. For a proton

$$\gamma_{Proton} = 2.675 \cdot 10^8 rad(s \cdot T)^{-1}$$

applies [16].

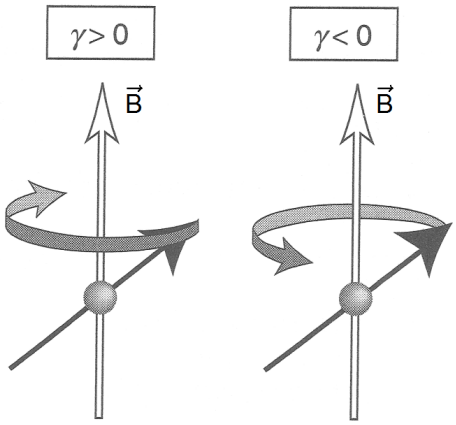

Figure 2.1.: Precession of spins with different γ values. Nuclei with a positive gyromagnetic ratio $\gamma > 0$ perform a counter-clockwise rotation, when looking in the direction of $\vec{B_0}$. The opposite is true for nuclei with $\gamma < 0$ [17, p. 30].

$$\hat{\mu} = \gamma * \hat{S}$$

Its sign determines if the spin angular momentum is parallel ($\gamma > 0$) or antiparallel ($\gamma < 0$) to the magnetic moment.

If we suppose a nuclei ensemble, the spin angular momentum can be visualized by a vector which indicates the axis of rotation. This vector can point in any direction of space. The distribution of the magnetic moments is therefore completely isotropic. However, the spins are affected when a magnetic field $\vec{B_0}$ is introduced. Their axis then describes a motion known as "precession[1]", where the rotational axis itself rotates around the external magnetic fields axis (which we will chose as our z-axis) enclosing a fixed angle.

This angle corresponds to the initial orientation of the axis of rotation relative to the z-axis. The precession speed, or rather precession frequency depends on the magnetic field $\vec{B_0}$ as well as on the gyromagnetic ratio γ. This frequency is referred to as "Larmor Frequency" ω $[rad/s]$.

[1]This motion has many parallels in classical physics. An example is the precession of the earths axis, because of the suns and moons gravitational field as well as the earths non-spherical shape. It can also be observed if a rotating tops axis is tilt.

$$\vec{\omega} = -\gamma \cdot \vec{B_0}$$

The Larmor frequencies sign specifies the direction of the spins rotation. This sign on the other hand depends on the gyromagnetic ratios sign, which means that with positive γ , which is the case for most nuclei, ω is positive, which results in a counter-clockwise rotation, when looking in the magnetic fields direction (see figure 2.1).

It has to be clear that the idea of spins as spinning and precessing microscopic tops is merely a model which suffices to describe the observed effect quite well.

2.2.1. Longitudinal magnetization

As mentioned above, when there is no external magnetic field, the direction of the spins is evenly distributed, which results in a total magnetic moment close to zero. When an external field $\vec{B_0}$ is turned on, the spins begin to precess around the fields axis[1].

This doesn't immediately change the isotropic property of the sample. However, this property is changed by different effects. The Larmor frequency depends on the total magnetic field surrounding the sample, which does not only consist of $\vec{B_0}$, but also of a rapidly varying microscopic field caused by magnetic particles like electrons and nuclei in rapid thermal motion. Therefore, two adjacent spins experience slightly different magnetic fields. The varying microscopic field causes a repeated change of the spins precession angle. This is only possible, because the spins precession period is on a time-scale of nanoseconds, which means that the spins executes millions of precession circuits, before the change of the precession angle, which can take as long as seconds, takes place. Although this influence seems random, it is slightly biased. Changing the spins orientation, it is more probable that the spin stays in a low magnetic energy state, which, for a positive γ , means parallel to the magnetic field. This ultimately causes a subtle disruption of spin isotropy.

[1] The protons Larmor frequency equals about 130 MHz supposing an external field of 3T.

This disruption however is the reason for a small net magnetic moment of the sample along the external fields direction and is the microscopic reason for paramagnetism. This magnetization is called "longitudinal magnetization"

Describing this process using quantum mechanics, the z-component of the spins may only take one of $2 * s + 1$ values. For protons $s = 1/2$ this implies either orientation along (parallel) or against (anti-parallel) the direction of the magnetic field $\vec{B_0}$. Because of the Zeeman effect, both states are associated with different energy levels, where states with lower energies, i.e. parallel to $\vec{B_0}$ are preferred. Using the Boltzmann distribution, it is possible to calculate the surplus of parallel spins:

$$\frac{N\uparrow}{N\downarrow} = e^{\frac{\gamma \cdot h \cdot B_0}{2 \cdot \pi \cdot k_B \cdot T}}$$

Assuming room temperature and $\vec{B_0} = 3T$, the surplus which is aligned parallel to $\vec{B_0}$ equals only about 20 ppm[1].

2.2.2. Transverse magnetization

Because the induced paramagnetism of the protons, which is proportional to $\vec{B_0}$, as well as the proton density and therefore characteristic for different tissue types, is about four orders of magnitude lower than the diamagnetism of the electrons, the longitudinal spin magnetization is very hard to detect.

Quantum-mechanically, the energy difference ΔE of the Zeeman levels is related to a frequency of a photon by the relation:

$$\Delta E = \hbar \omega_0$$

This frequency matches the previously introduced Larmor frequency. Using radiofrequency pulses of this very frequency, it is now possible to induce transitions between the Zeeman levels, disrupting thermal equilibrium. As the equilibrium is again established, the previously absorbed energy is emitted and can be measured.

[1] Assuming $\vec{B_0} = 7T$ the surplus equals about 50 ppm

In the classical model, we think of "transfering" the longitudinal magnetization into the perpendicular plane instead of measuring it in the direction of the external field. Although, when in thermal equilibrium most of the precessing spins posses a component perpendicular to the external magnetic field, no net magnetization can be observed. This is because the total magnetization is cylindrically symmetric around the direction of the $\vec{B_0}$ field.

One can think of the protons as spinning tops which are precessing around the z-axis. A radiofrequency (rf) pulse with Larmor frequency, applied perpendicular to $\vec{B_0}$, now pushes their axis in a more horizontal position, which depends on the strength and duration of the pulse. For example, it is possible to apply a 90° pulse, which rotates the z-component of the magnetization completely into the transversal plane and therefore causes a transversal magnetization.

Because every spin is rotated by the same angle, the net magnetization of the sample is rotated too, which means that instead of being aligned along the z-axis it is now perpendicular to the external magnetic field. This net magnetic moment is now called "transverse magnetization". Since every spin still precesses around the external $\vec{B_0}$ field with a given angle, the net magnetic moment located in the xy-plane precesses too. The frequency of the macroscopic magnetization's rotation perpendicular to the external field equals the Larmor frequency and the magnetization's course can be therefore described as:

$$M_x(t) = M_x(0) \cdot sin(\omega \cdot t) \cdot e^{-t/T_2}$$

$$M_y(t) = -M_y(0) \cdot cos(\omega \cdot t) \cdot e^{-t/T_2}$$

or

$$M_{xy}(t) = M_{xy}(0) \cdot e^{-t/T_2}$$

respectively.

The reason for the transversal magnetization decay lies in the microscopic fluctuating fields which cause a dephasing of previously aligned spins. The

constant T2, which describes the decay[1] of the precessing macroscopic magnetization is known as "transverse relaxation time constant" or "spin-spin-relaxation time constant". The last term is misleading, because the net magnetization loss is not dependant on spin interaction, but only on inhomogeneous magnetic fields, which cause different spins to precess with different frequencies and therefore lose coherence.

Due to the external field and the effects discussed above (see section 2.2.1) the longitudinal magnetization builds up again after the rf-pulse and can be described with the following formula

$$M_z(t) = M_z(0) \cdot (1 - e^{-t/T_1})$$

where the constant T1 is the so called "spin-lattice" or "longitudinal relaxation time constant". While the use of the term "lattice" origins from times where NMR was mainly performed on solids, longitudinal refers to the orientation of the net magnetization build-up which is, as already mentioned, parallel to the external magnetic field.

The transversal magnetization decay is not related to the spin lattice relaxation. These are two separate phenomena. None the less the longitudinal magnetization builds up, while the transversal magnetization decays over time after the rf-pulse (see figure 2.2).

The macroscopic magnetization precessing in the xy-plane after the rf-pulse is, like the longitudinal magnetization before the pulse, very small. Nevertheless it is detectable because it precesses at a very specific (Larmor) frequency. A rotating, i.e. changing magnetic field B, caused by a rotating magnetic moment, causes a rotating electrical field E[2] which in turn produces an oscillating current if a coil is placed appropriately nearby. This NMR signal is also called "Free Induction Decay (FID)" and forms the basis for all NMR applications [17].

In summary, there are three basic steps conducted by a NMR spectrometer:

1. Magnetizing a spin ensemble with the use of a strong magnetic field

[1] T_2 measures the time after excitation at which transversal magnetization is reduced to $1/e$ of its initial value.

[2] Maxwell-Faraday equation: $\nabla x \vec{E} = -\frac{\partial \vec{B}}{\partial t}$

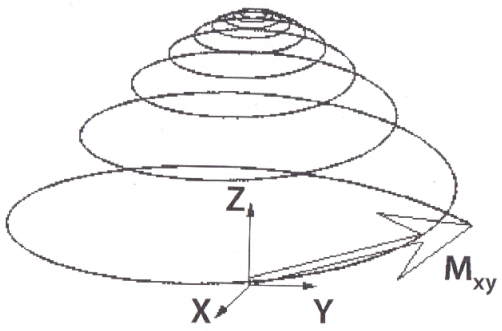

Figure 2.2.: The magnitization precesses around $\vec{B}_0$ and is rotated into the transversal plane. While the spins dephase transversally, the magnetization builds up longitudinally.

2. Flipping the longitudinal net magnetization into the xy-plane (causing transversal magnetization) with the use of a rf-pulse

3. Measuring the oscillating currents induced by the transverse precessing magnetization with the use of a coil [17]

Only receiving the MR-signal as described does not produce a picture yet so additional steps are needed. The MR-signal is acquired of little volumes (voxels) by superimposing magnetic gradient fields on the static $\vec{B}_0$ field. Precession frequency ω is dependent on the total magnetic field and therefore different for every location if linear gradient fields are overlaid. A Fourier analysis makes it then possible to assign a specific position to every frequency. This procedure is discussed in the following section in detail.

2.2.3. Image reconstruction and k-space

To create an image it is necessary to encode the spatial position of the signal. This can be done by altering the Larmor frequency of each position in the sample with the use of spatially variant (gradient) magnetic fields. If we introduce such a field the static field $\vec{B}_0$ changes to a spatially variable field $\vec{B}$ which is given by

$$\vec{B} = \vec{B}_0 + \vec{G} \cdot \vec{r} = -\frac{\vec{\omega}}{\gamma}$$

where $\vec{G}$ is the strength of a gradient field, $\vec{r}$ is the position in space and $\vec{B_0}$ is the constant field which would be there disregarding the gradient field. As γ is a constant, the Larmor frequency ω is proportional to the strength of $\vec{G}$. This means that the stronger the gradient $\vec{G}$, the higher the difference of ω between adjacent spins. This makes it possible to resolve smaller positional differences, which in turn leads to a higher possible resolution (i.e. smaller voxels).

If we now describe the course of magnetization of a single excited spin as

$$M = M_0 * e^{-i\omega t}$$

and substitute ω according to the Larmor frequencies formula, we get

$$M = M_0 * e^{-i\gamma B_0 t}$$

The induced signal of a voxel is proportional to the change of magnetization, i.e. dM/dt and therefore given as

$$S(t) = C * M_0 * e^{-i\gamma B_0 t}$$

If we now substitute the static $\vec{B_0}$ with the above mentioned variable field, we get

$$S(t,\vec{r}) = C * M_0 * e^{-i\gamma(B_0+\vec{G}\cdot\vec{r})t}$$

which is equivalent to

$$S(t,\vec{r}) = C * M_0 * e^{-i\gamma B_0 t} + e^{-i\gamma\vec{G}\cdot\vec{r}t}$$

The term $e^{-i\gamma B_0 t}$ can also be written as $e^{-i\omega t}$ and represents an oscillation of Larmor frequency. As $e^{-i\omega t}$ is independent of location one can correct for this signal modulation of known frequency and it is therefore ignored below. This yields

$$S(t,\vec{r}) = C * M_0 * e^{-i\gamma\vec{G}\cdot\vec{r}t}$$

for the induced signal of a single spin with magnetization M_0 at position $\vec{r}$.

The joined signal of a spin ensemble is now given as

$$S(t) = C * \iiint_V M(\vec{r}) * e^{-i\gamma\vec{G}\cdot\vec{r}t}\,\mathrm{d}\vec{r}$$

We now substitute $\gamma\vec{G}t$ with a new variable $\vec{k}$, which is related to the different gradients in such a way that

$$k_x = \gamma G_x t$$

$$k_y = \gamma G_y t$$

$$k_z = \gamma G_z t$$

and obtain

$$S(\vec{k}) = C' * \iiint_V M(\vec{r}) * e^{-i\vec{k}\cdot\vec{r}}\,\mathrm{d}\vec{r}$$

It is possible to invert the last equation, because it equals a Fourier transformation. This yields

$$M(\vec{r}) = C'' * \iiint_k S(\vec{k}) * e^{i\vec{k}\cdot\vec{r}}\,\mathrm{d}\vec{k}$$

where $M(\vec{r})$ is the MR-signal dependent on image space coordinates and $S(\vec{k})$ represents the signal dependent on coordinates of the frequency domain, i.e. k-space. This equation makes it possible to transform the frequency encoded signal, which resides in the temporal domain into the spatial domain and therefore obtain an image

As described above, we need three gradient fields in order to encode a three dimensional spatial position. These fields do not only differ in their orientation (they are perpendicular to each other), but also in their duration and length.

Slice selection gradient

Because of the first gradient field only spins in a certain slice precess with the Larmor frequency affected by the rf-pulse. Therefore only spins of this specific

slice are flipped into the transversal (xy-) plane by the radio-frequency-pulse. To achieve this, the slice selection gradient has to be active at the same time as the rf-pulse. As the pulse does not only affect a single frequency, the slice thickness is determined by the bandwidth of the rf-pulse as well as the strength of the gradient field.

Phase encoding gradient

After selecting a certain slice, the positions in the xy-plane have to be encoded. Before the signal is measured, the second gradient (in our case aligned to the y-axis) is applied. While the phase encoding gradient is active affected spins experience a change in frequency. Thus when the gradient is switched off again, each of the spins oriented along the y-axis rotated by a different amount. In other words: the phase of the spins is varied by applying a gradient field for a short time. By repeating this step using y-axis gradient fields with different strength, the phase of each spin changes differently every time. Because changes in phase equals a frequency and every spin experiences different phase changes the spins spatial position along the y-axis is frequency encoded.

Frequency encoding gradient

At last the so called frequency encoding gradient is applied. This gradient field, in our case along the x-axis, is turned on during signal acquisition (thus it is also referred to as the "readout-gradient"). Spins along the x-axis now precess with different frequencies and therefore also emit electromagnetic radiation of different frequencies. Since the slice selection gradient limits the measurable signal to a single slice, a two dimensional Fourier transformation is now used to convert the recorded data from the frequency to the spatial domain [18, 19].

Figure 2.3 illustrates the gradients, figure 2.4 gives an overview of the rf-pulse and gradient timing, while figure 2.5 shows an axial brain slice in both k-space and image space.

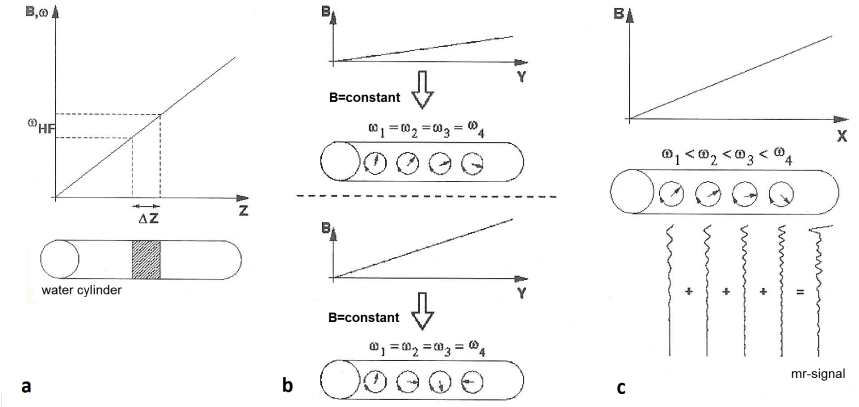

Figure 2.3.: Illustration of space encoding **a** Slice selection: Only protons in a slice with thickness Δz are excited by the rf-pulse. **b** Phase encoding: A short gradient field activation leads to a phase difference between the spins. The stronger the gradient, the bigger the phase difference. **c** Frequency encoding: The gradient field activation during data acquisition leads to a variation of the Larmor frequency dependent on spatial location along the gradient axis. **a-c** are carried out after each other. The whole procedure has to be repeated for different strengths of the phase encoding gradient. The measured signal is the sum of all spin signals, which all possess a unique frequency and phase combination. Adapted from [19, p. 67].

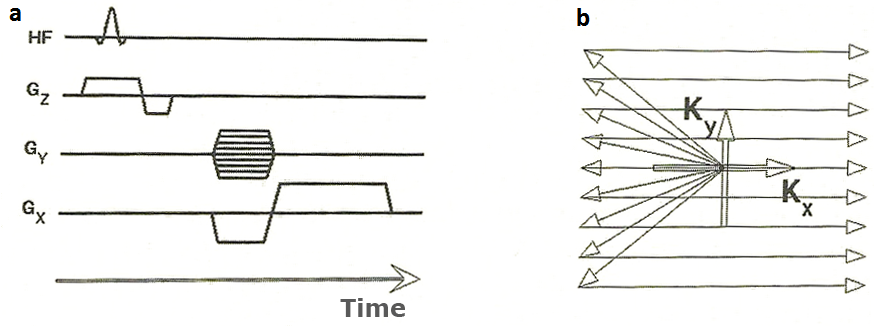

Figure 2.4.: a Time dependent activation of the rf-pulse, denoted as high-frequency (HF) pulse, slice selection gradient (G_Z), phase encoding gradient (G_Y) and frequency encoding gradient (G_X). The multiple lines at the phase encoding step hint at the repetition of the whole sequence for each of the different phase encoding gradients **b** Every repetition of the sequence with different G_Y represents a row in k-space. The MR-signal is only recorded during the frequency encoding gradient. One row in k-space is filled with data (Arrows from left to right) during one repetition. Each row contains data from the whole volume [19, p. 68].

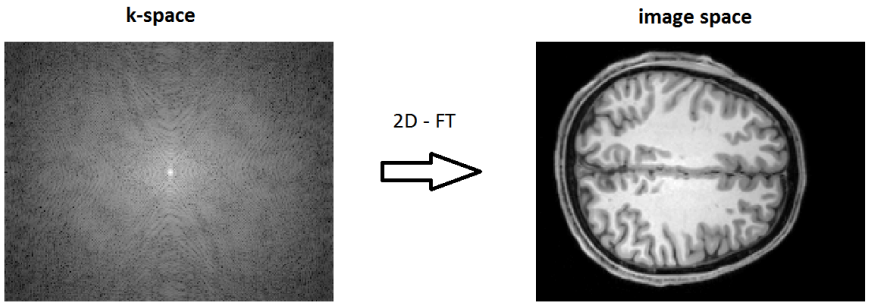

Figure 2.5.: On the left an axial brain slice in k-space can be seen. On the right the same image is shown after two dimensional Fourier transformation. The data now resides in the image space.

2.2.4. MRI contrasts

T_1 and T_2 weighted images differ quite strongly from each other. T_1 weighted pictures, which are produced by reducing the repetition time between the high-frequency pulses (TR) and echo time (TE) cause regions not to fully "recover" from an excitation pulse before experiencing the subsequent pulse, are picturing fat tissue bright while picturing liquids dark. T_2 weighted pictures are picturing liquids bright and fat tissue with medium brightness.

2.2.5. Spin echoes

An additional reason for signal decay is found in the inhomogeneity of the static magnetic field $\vec{B_0}$ which is caused by the scanner design and the magnetic properties of the sample, respectively the patient. These static, local inhomogeneities appear at locations with changing magnetic properties, for example along borders between different tissues. Effectively increasing the rate of signal decay these static inhomogeneity effects can be described by T_2' which adds to T_2 to give the effective T_2 or T_2*:

$$\frac{1}{T_2*} = \frac{1}{T_2} + \frac{1}{T_2'}$$

Therefore the MR-signal decays with time constant T_2*. The spin-echo sequence makes it possible to compensate for T_2' effects. After $TE/2$, with TE

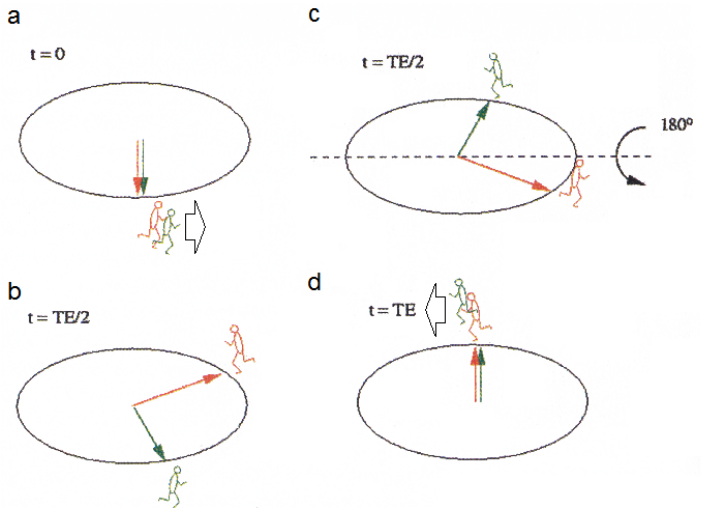

Figure 2.6.: Illustration of the Spin Echo. a,b) Starting the race, participants are running with different, but constant speeds. c) After $TE/2$ a 180° rf-pulse is applied, which converts every advantage into a disadvantage. Thinking of spins, this means that the higher the precession frequency of a certain spin is, the more it will be set back at due to the pulse. d) After "Echo Time" TE has elapsed all of the participants finish the race simultaneously. Adapted from [19, p. 70].

being the "Echo Time", spins are flipped using a 180° rf-pulse. Spins experiencing higher magnetic fields and thus higher precession frequencies will be flipped back more than slower rotating spins. After TE all phase differences will be compensated and the signal strength reaches a maximum again (see figure 2.7). Eliminating the T_2' decay, the time in which the signal fades away is the transverse relaxation time constant T_2. The signal decay dependent on T_2 can not be reversed because it depends on random microscopic field inhomogeneities (see chapter 2.2.2).

One can compare the 180° pulse and his effect to a race were the participants are running with different, but constant speeds (see figure 2.6). After $TE/2$ every advantage is converted to a disadvantage and after the "Echo Time" TE has elapsed all of the participants finish the race simultaneously.

The spin-echo sequence helps to improve the MRI quality by removing T_2' effects, but as T_2' is strongly dependent on magnetic property changes of the probe, such as varying blood oxygenation, BOLD-fMRI studies mostly use T_2*-weighted sequences.

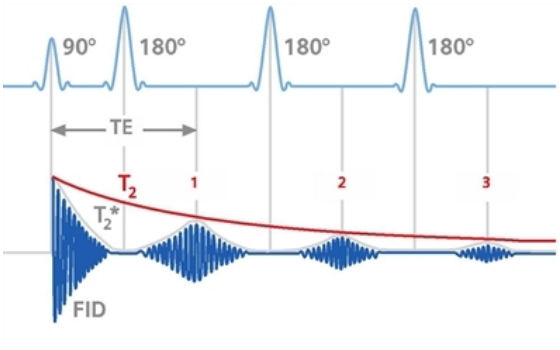

Figure 2.7.: Applying several 180 degree pulses, the T_2' effect can be suppressed, which makes the signal decay only depend on T_2 and leads to several spin echoes [20].

2.2.6. Echo planar imaging (EPI)

This technique, developed by Peter Mansfield (*1933) in 1977, allows for imaging a plane within 30ms - 100ms. In its single-shot variant spatial encoding of the x-y-plane occurs after a sole 90-degree pulse and because of the small T_2*, very fast gradient switching is required to image the whole plane in that time. Rapid gradient switching, however, is accompanied by high levels of acoustic noise. EPI is of highest importance for functional MRI and enables fMRI with high temporal resolution. Nevertheless the spatial resolution is typically limited to about 128x128 pixels per plane and quality losses are experienced if EPI is compared to other imaging sequences. In fMRI studies it is therefore common to perform a structural MRI with high spatial resolution in addition to EPI [18].

Even faster imaging, or more recorded slices in the same time, can be achieved by using parallel imaging methods [21, 22].

2.2.7. Parallel Magentic Resonance Imaging (pMRI)

PMRI can enhance practically every MRI method by reducing image acquisition time using conventional gradients. This is of particular importance, because faster imaging can improve spatial and temporal image resolution allowing for more precise insights in anatomical structures and functional processes.

Current receiver coils consist of multiple surface coils, which cover a certain

volume. Inherent spatial sensitivity information of these surface coils can be derived during the patient setup by a so called prescan. Another option is the so called autocalibration, which refers to a few additionally measured k-space lines for every subsequent pMRI experiment. By exploiting this information it is possible to reduce the need for spatial encoding. Because the number of necessary phase-encoding steps is reduced, accelerated imaging is now possible. Using head coils with 32 independent channels, imaging could be theoretically accelerated by a factor of 32. Due to image quality requirements a lower, one-digit, factor is most commonly used.

To keep things simple the Cartesian-type sampled k-space is assumed. This means a reduction of the number of phase-encoding steps by a reduction factor R is achieved by increasing the distance of equidistantly sampled k-space lines. On the other hand, the maximal k-values are left unchanged in order to maintain resolution. In image space, this type of kspace undersampling translates to a reduced field of view (FOV) in phaseencoding direction, which is associated with foldover artifacts.

A simplified example

Assume an array of $N_c = 2$ independent receiver coils, of which each covers one half of the FOV in phase-encoding direction (see figure 2.8 (b)). The coils possess a boxcar-type sensitivity profile C_k. In our example, coil 1 measured the top half (see figure 2.8 (c)), while coil 2 measures the bottom half of the object(see figure 2.8 (d)).

Imaging using just a single homogeneous volume coil, we would need N phase-encoding steps for acquiring full FOV coverage of the object (see figure 2.8 (a)). Using the illustrated two coil setup, both coils provide full FOV images, but their signal intensity corresponds to the mentioned boxcar sensitivity profiles. This means that while each coil records a full FOV image, coil 1 only images the top part of the object and receives no signal from the bottom part. The opposite is true for coil 2.

Exploiting this fact, we can half the FOV and therefore reduce the phase-encoding steps by the factor $R = 2$. In our case, imaging time is therefore

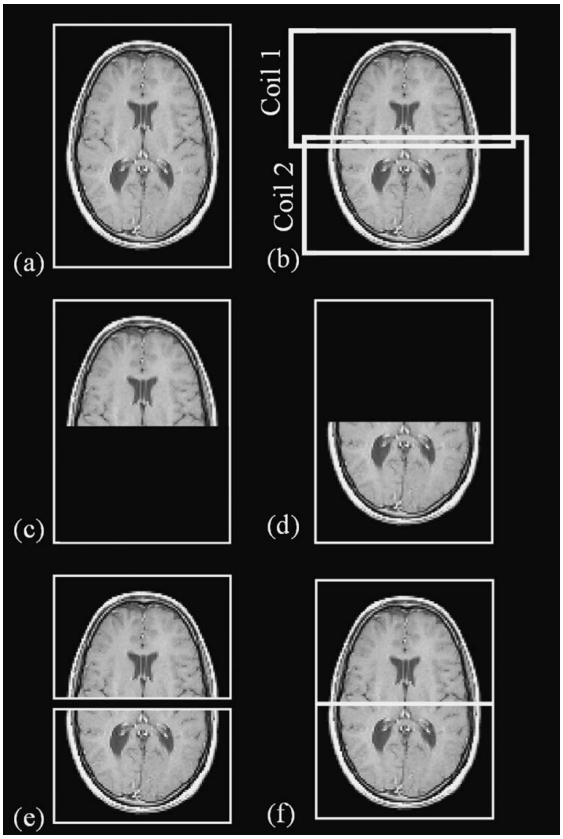

Figure 2.8.: (A) Full FOV image obtained by one homogeneous coil, using N phase-encoding steps. (B) Two-coil array with boxcar-type sensitivity. (C) Full FOV image with N phase-encoding steps obtained by coil 1. (D) Full FOV image with N phase-encoding steps obtained by coil 2. (E) FOV/2 image with N/2 phase-encoding steps received in coil 1 (top) and in coil 2 (bottom). (F) Combined coil images with full FOV and N/2 phase-encoding steps [21].

halved, because both coils acquire a half FOV image simultaneously (see figure 2.8 (e)). Parallel imaging is thus made possible by the distinctiveness of coil sensitivities.

By shifting the individual coil images, they are finally combined to one full FOV image. (see figure 2.8 (f)). While the final image is acquired in half of the time, the resulting signal-to-noise ratio (SNR) is decreased by a factor $\sqrt{R}$. This is because the number of phase-encoding views which contribute to the image is reduced by a factor R.

In the real-world however, coil sensitivities C overlap to some extent and are smoother over the FOV, which makes the whole procedure more complicated. Still, the following requirements have to be fulfilled in order perform to pMRI [21]:

- Multiple receiver coils featuring different coil sensitivities over the FOV are necessary.
- Each coil has to possess its own receiver pathway.
- An accurate knowledge of the coil sensitivities is required for pMRI reconstruction.

SENSE

SENSitivity Encoding (SENSE) is a pMRI reconstruction method, which takes place in the image domain and can be described as "unfolding" algorithm.

In the previous section we saw that pMRI accelerated imaging leads to a FOV reduction of every component coil image. The component coil images of each coil are weighted with coil sensitivity C and because of the reduced FOV folding of the data is experienced in the phase encoding direction. The pixels of these images do not translate one-to-one, but rather contain information of multiple (R) pixels of the final, full FOV image.

SENSE allows for "unfolding" these images and assigning the correct image part of each coil to the full FOV image by using the coil sensitivity data from a reference scan, which is performed prior to data acquisition [21].

GRAPPA

GeneRalized Autocalibrating Partially Parallel Acquisitions (GRAPPA) refers to a self-calibrating pMRI method, which, in contrary to SENSE, performs the "unfolding" in the k-space domain.

An additional difference to SENSE, which performs a preliminary reference scan, is that GRAPPA uses autocalibration signal (ACS) k-space lines during the scan in order to estimate coil sensitivities.

In order to reconstruct the full FOV image, GRAPPA uses multiple k-space lines from all coils to fit a single component coil ACS signal. Repeated for every coil, this procedure makes it possible to calculate missing k-space lines and results in uncombined coil images of the component coils, which can then be joined by using a sum of squares approach [21].

2.2.8. Basics of fMRI

In order to perform functional imaging a contrast between active and resting regions is necessary and most often achieved by Blood Oxygenation Dependent (BOLD) - weighted MRI. Blood transports oxygen through the hemoglobin molecule, which contains iron atoms and changes its magnetic properties if oxygen is bound to them. The molecule is then called oxyhemoglobin and has diamagnetic features like the surrounding tissue, whereas without oxygen bound to it the molecule is named deoxyhemoglobin and is paramagnetic. The variation of the blood's magnetic properties compared to the surrounding area then causes the fMRI signal to decrease, i.e. the proton spins to dephase faster and therefore a lower T_2*. In order to observe the difference regarding signal decay caused by different T_2* constants of the tissue influenced by deoxygenated blood, some time has to elapse. Hence, if we chose a very short TE we receive a lot of signal, but BOLD contrast is poor.

One would think that active neurons consume oxygen and that the deoxyhemoglobin molecules would increase magnetic field inhomogeneity and therefore lower the MR-signal, but it is quite the contrary. The increased demand of energy in activated regions is compensated by an increase in glucose supply through a rise in arterial blood flow. As this type of blood also carries

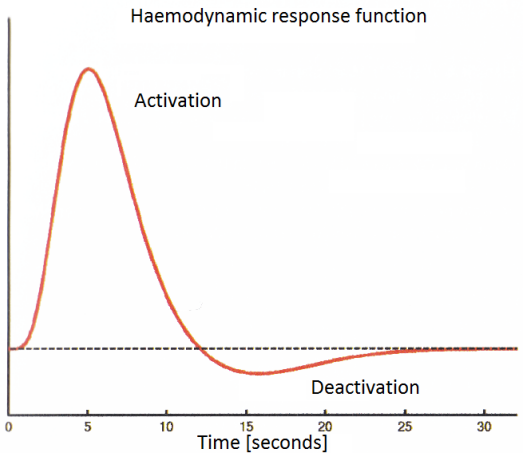

Figure 2.9.: Haemodynamic respone function. Adapted from [19, p. 77]

an increased number of oxygenated hemoglobin and oxygen consumption rate increases only marginally in activated regions of the brain, blood oxygenation and thus signal intensity in this regions rise [23,24]. The recorded BOLD signal primarily measures the input and processing of neuronal information within a region and not the output signal transmitted to other brain regions. [25].

The BOLD signal peak occurs approximately four seconds after neuronal activation and is often followed by a signal undershoot [26]. This is what we call hemodynamic response function (see figure 2.9).

Because of the relatively small magnitude of the BOLD effect, a relatively low resolution has to be used, so more protons can contribute to a single voxel.

Various techniques may be used for assessing the BOLD effect, most simply taking the difference between the acquired images in active and resting states.

Because arteries and arterioles contain highly oxygenated blood regardless of the increased blood flow in a specific region, the increase of oxyhemoglobin molecules in a given area is mainly observed in veins and smaller veneoles. This fact can lead to image artifacts caused by large veins leading back to the torso which have to be taken into consideration interpreting an image.

3. The human visual system

This chapter will give a brief overview on the human visual system. In order to perceive visual stimuli, they have to be transformed in various ways after entering the eye.

First, the light is focused by the cornea and lens, to build the retinal image. The different photoreceptors located in the retina then transform this image into neural responses. Following visual pathways, these neural responses are reorganized and transformed several times until they form cortical representations of the perceived image [27, p. 13].

3.1. The human eye

Figure 3.1 gives an overview of the different components of the eye.

3.1.1. Cornea & Lens

When light enters the eye it is focused onto the photoreceptors by the cornea and lens. The transparent cornea covers and protects the inner parts of the eye, like iris and lens. Compared with the lens, the focus-fixed cornea has a higher focusing power. Of the total optical power of the eye (about 60 diopters[1]) the cornea, due to the aqueous humour, accounts for about 40 dpt [27, p. 34] [29].

While the refractive power of the lens is inferior to the corneas, the lens can adjust its focus to account for the object's distance. This procedure is known as "accommodation". With the help of the ciliary muscle, the lens can be thickened and thus improve its refractive power, which is necessary if the

[1] 1 dpt = 1/m

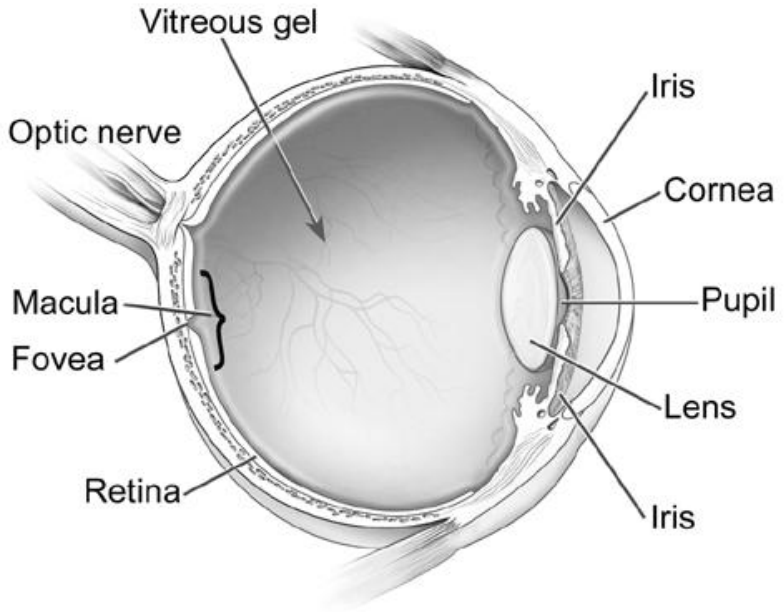

Figure 3.1.: Overview of the imaging components of the eye [28].

focused object is nearby. Relaxation of the ciliary muscle on the other hand leads to a flattened lens and therefore to lower refractive power and a higher focal distance [30, p. 713-715].

3.1.2. Retina

After passing the cornea, pupil, lens and the vitreous gel, the already focused light reaches the retina. The retina is a light sensitive layer of neural tissue that covers the inner eye. The retina itself consists of multiple layers and cell types and light has to pass through all this layers before being absorbed by the photoreceptors. This section will focus mainly on neural pathways and not on the histological composition of the retinal layers. Figure 3.2 illustrates this neural connections [27,30].

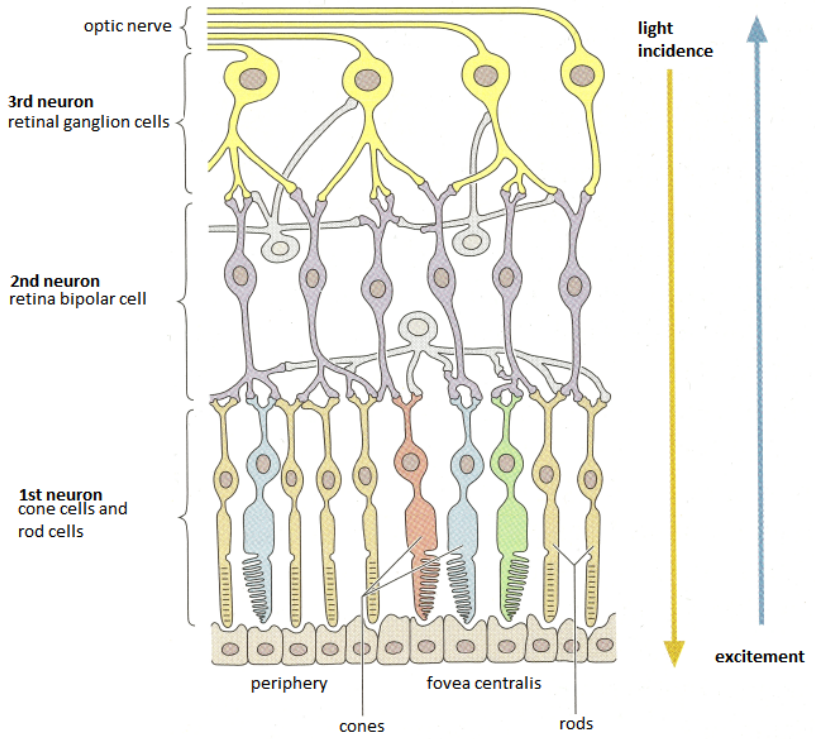

Figure 3.2.: Neural pathways in the human retina. Adapted from [30, p. 717].

Photoreceptors

The two fundamentally different photoreceptors which are important for image recognition in the human eye are "rods" and "cones"[1].

After passing the previous retinal layers a fraction of the light which entered the eye will make its way through the inner segment of the photoreceptors. In the outer segment, the photons are then either transformed into neural impulses with the use of a photopigment[2], or pass through and exit the photoreceptor at the other side.

Rod cell Rod cells are more common and light sensitive than cone cells. Because rods are so light sensitive, one photon is sufficient for generating

[1] A third type of photoreceptors are photosensitive ganglion cells. These cells are, among other things, responsible for regulating the circadian rhythm [31].
[2] Rhodopsin for rod cells. Iodopsin for cone cells.

a detectable response [32]. The approximately 100 million rods in each eye are mainly responsible for scotopic vision, which means seeing under poor light conditions, and only allow for monochromatic vision. There are no rods present in the fovea (see figure 3.1 and 3.3), the part of the retina where the center of the visual field is projected on. Very dim light sources, such as weak starlight, are therefore better perceived by peripheral vision.

Although rods allow us to see much better under scotopic light conditions, their visual acuity is poor when compared to cone cells. The reason for the enhanced sensitivity, but reduced specificity and therefore reduced perceived detail, is their "many to one" behavior. Many rod cells converge to a single neuron in the retina [27, p46-47].

Cone cell In contrast to rod cells, there are only about five million cone cells. Cones work best under higher, photopic, light levels. These cells are made up of three different subtypes; l-, m- and s-cones, which have their spectral sensitivity peak at long, middle and short[1] wavelength respectively. The different wavelength selectivity of the cone types and their analog behavior allow us to see different colors.

Cones are generally larger and less tightly spaced when compared to rods, but the spacing near the fovea is an important exception. Although cone cells are the less common photoreceptors, there is a huge conglomeration of about 50.000 cones in the fovea centralis. That is why this region is the one with the highest visual acuity in the retina (see figure 3.3).

The signals from one cone are encoded by several neurons. This means that, contrary to rod cells, cones and optic-tract neurons follow a "one to many" relationship [27, p46-48].

Neural cells and connections in the retina

As seen in figure 3.2, there are intermediate steps between light transformation by photoreceptors and further transfer of the image signal into the brain by

[1]The terms long, middle and short are relative to the electromagnetic spectrum visible by humans, i.e. 400nm-800nm.

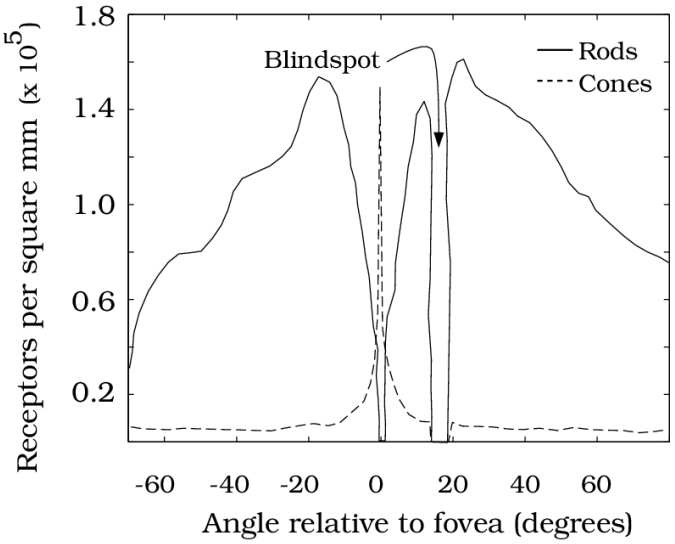

Figure 3.3.: Rod and cone density in relation to their distance from the fovea in degrees of visual angle [27, p. 46].

the optic nerve. The retinal neurons can be classified into five basic categories. Besides the already discussed photoreceptor cells, there are horizontal cells, bipolar cells, amacrine cells and retinal ganglion cells.

The photoreceptors are connected to horizontal and bipolar cells. While horizontal cells connect different photoreceptor cells and bipolar cells[1], bipolar cells transfer the image signal to the ganglion cells, which means that all visual signals must pass through them. Photoreceptors and bipolar cells are also referred to as the first and second neuron, respectively.

Amacrine cells connect bipolar as well as ganglion cells horizontally and are therefore similar to horizontal cells.

Axons of the retinal ganglion cells, which are also known as the third neuron, deliver the only output signal of the retina. They exit the eye at the optic disk and form the optic nerve. Because of the absence of rod and cone cells at the optic disks location, the region is also called "blind spot". This blind spot is not noticed by us since the other eye compensates for this deficit [27, p. 111-114] [30, p. 717-720].

[1] "many to one" and "one to many" relationship, see above

3.2. Parvocellular & Magnocellular pathway

Visual streams or pathways are connected series of neurons, which carry information in parallel. The parvo- and magnocellular pathway, which will be discussed in the following include the majority of the retinal output.

The different streams are assigned to different ganglion cell types. For the parvocellular pathway the corresponding cells are the so called "midget cells", while "parasol cells" are associated with the magnocellular pathway. The midget cells dendritic field is compact and dense when compared to parasol ganglion cells, whose dendritic field is larger and scarce. Near the fovea, midget cells connect to only one bipolar cell which then connects to a single cone cell. Moving away from the foveal area the dendritic field diameter grows slowly for both types of cells[1]. Midget as well as parasol cells are present at every location of the retina and therefore a complete image is obtained by both of them. Former encode at high resolution of up to 60cpd[2], which matches the sensitivity of the photoreceptors, while latter encode at a lower resolution of up to 20cpd. The reason lies in the size of the dendritic field. Midget cells are able to deliver a higher resolution, because of their smaller dendritic field diameter, which gathers signals from a relatively small part of the retina. Because both cell types cover the retina completely, midget cells are seven to nine times more common than parasol cells [27, p. 118-122].

3.2.1. Optic chiasm

After leaving the eyes, most of the optic nerves fibers cross at the optic chiasm. There the image information is reorganized regarding the left and right visual hemifield. Information originating from the left visual hemifield of both eyes is passed on to the right lateral geniculate nucleus (LGN), a structure located in the thalamus, while information originating from the right visual hemifield is passed on to the left LGN [27, p. 157].

[1] Midget cells have a diameter of about 5µm at the fovea and about 200µm at the periphery. Parasol cells have a diameter of about 30µm at the fovea and about 600 µm at the periphery.
[2] Cycles per degree is a unit for measuring angular resolution.

3.2.2. Lateral geniculate nucleus

The majority of the retinal ganglion cell's axons are sent to the LGN layers. Each of the human LGN consist of six layers, which can be classified by the visual stream and eye they receive input from. Axons from midget cells end in the four superficial layers which are called "parvocellular layers" and are build up of neurons with small cell bodies. The two deeper layers have neurons with bigger cell bodies and are called "magnocellular layers". This is where the axons of the parasol cells end. Between these two regions, in the intercalated layers, there are koniocellular cells receiving their input from other retinal ganglion cells, so called bistratified cells [33].

The visual stream, which begins with the midget ganglion cells and ends in the parvocellular layer of the LGN is called "parvocellular pathway", while the stream which begins with the parasol cells and ends in the magnocellular layer of the LGN is called "magnocellular pathway".

Now, are there also functional differences between these two visual streams? Damage in the LGN parvocellular layers of monkeys, which include over 70% of the retinal ganglion cells, caused an impairment regarding color discrimination, pattern detection and stimuli which have high spatial and low temporal frequency in general. Disrupting the magnocellular layers did not show this obvious failures, but on closer examination one could see a change for the worse in stimuli related to high temporal frequency and low spacial frequencies, such as rapidly flickering targets. This kind of information also needs to be processed when detecting and tracking movements. Interestingly, monkeys could compensate for the damage done in one pathway by increasing the others quality of information [34].

Layers of the LGN are not only classified by the type of visual pathway they receive their input from, but also by their eye of origin. While layers 1,4 and 6 receive their input from the retina located on the same side of the head, layers 2,3 and 5 receive input from the opposite side.

The distance of the ganglion cells from the fovea is also reflected in the neurons organization in the LGN. While the back of the LGN is responsible for visual signals originating from neurons which receive input from retinal

regions near the fovea, the ganglion cells which are placed further away from the fovea send their output to the frontal regions of the LGN.

The visual stream originating from the LGN and ending at the primary visual cortex is also called fourth neuron [27, p. 123-127].

3.3. Visual Cortex

The occipital lobe is the center of visual processing. It houses the visual cortex which is the main target of visual signals coming from the retina and LGN. The primary visual cortex is also called "area V1" and its neuron number is about hundredfold, when compared with the LGN. In contrast to animals which can more or less recover from a lesion in this area, humans lose almost all abilities related to vision when this $\sim$24 cm^2 large area is damaged. The primary visual cortex is made up of six different layers, which receive signals from different LGN layers.

Input from the intercalated layers of the LGN are received by layers 2 and 3 [35], which mainly consist of cell bodies and local dendritic connections. The output of this layers is then send to different layers of the cortex. Together with layer 1, this layers form the so called "superficial layers".

Layer 4 is subdivided into four parts. Layers 4A, 4B, 4Cα and 4Cβ.

Layer 5s output mainly targets a part of the midbrain, while layer 6 is sending a lot of information back to the LGN [36].

As mentioned in section 3.2.1 the visual information gathered by the retinae is seperated with respect to the visual hemifields. This means, that areas V1 in both hemispheres receive signals from both eyes, but the visual cortex located in the left hemisphere only receives visual information from the right hemifield, while the right hemisphere only receives information from the left one.

Similar to the LGN, there are also other factors determining the signals target region in the visual cortex. After the hemisphere is decided by the hemifield the stimulus is perceived in, the eye of origin, class of ganglion cell and spatial position of the ganglion cell within the retina are factors by which the connec-

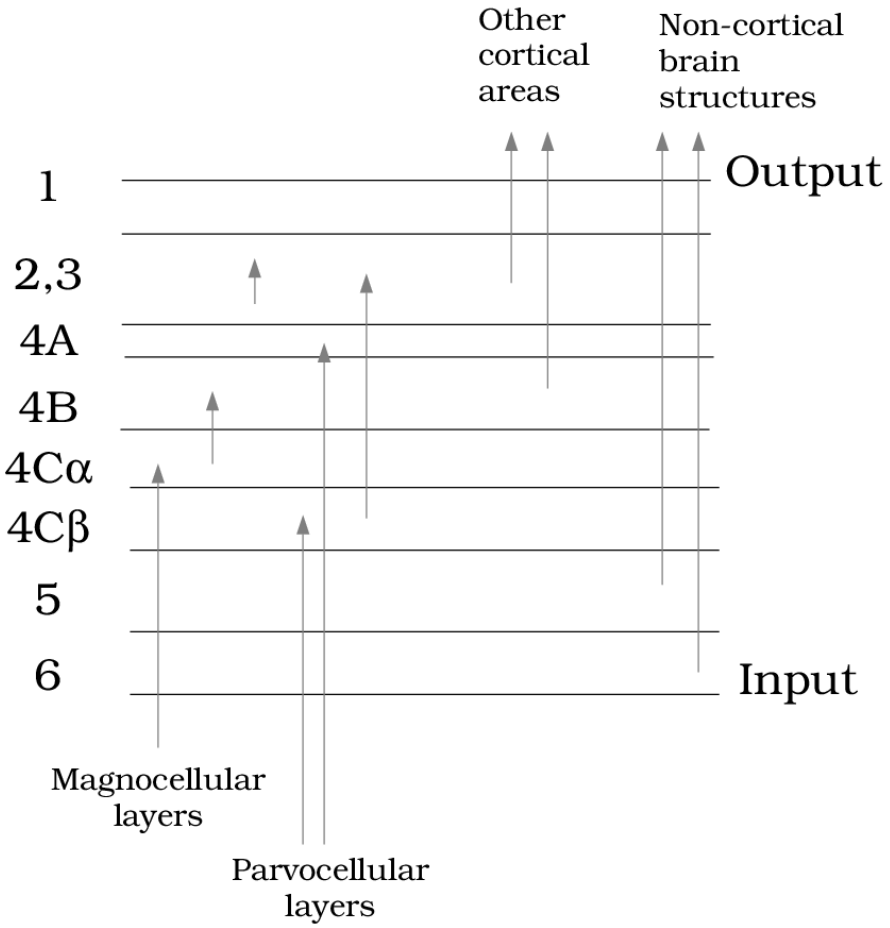

Figure 3.4.: Neural inputs and Outputs of area V1. [27, p. 156].

tions to the visual cortex are organized. These dependencies will be discussed in the following paragraphs.

The separation of the LGN regarding the eye of origin (see section 3.2.2) is continued in the cortex. Observing layer 4C, one can see that signals from different eyes are send to different bands in V1. These bands are referred to as "ocular dominance columns" [37] and span about 800-900 µm in humans [38]. This does not mean that every neuron receives input from one eye only. In superficial layers of the primary visual cortex, most of the neurons are obtaining input from both eyes and are called binocular neurons. The development of these neurons depends heavily on experiences during maturation. Animal studies showed that if one eye is is covered during a critical period of time

in development, the animal remains blind in this eye forever [39]. Figure 3.5 illustrates the organization of the pathways leading from the eyes to the layers of the left LGN and visual cortex.

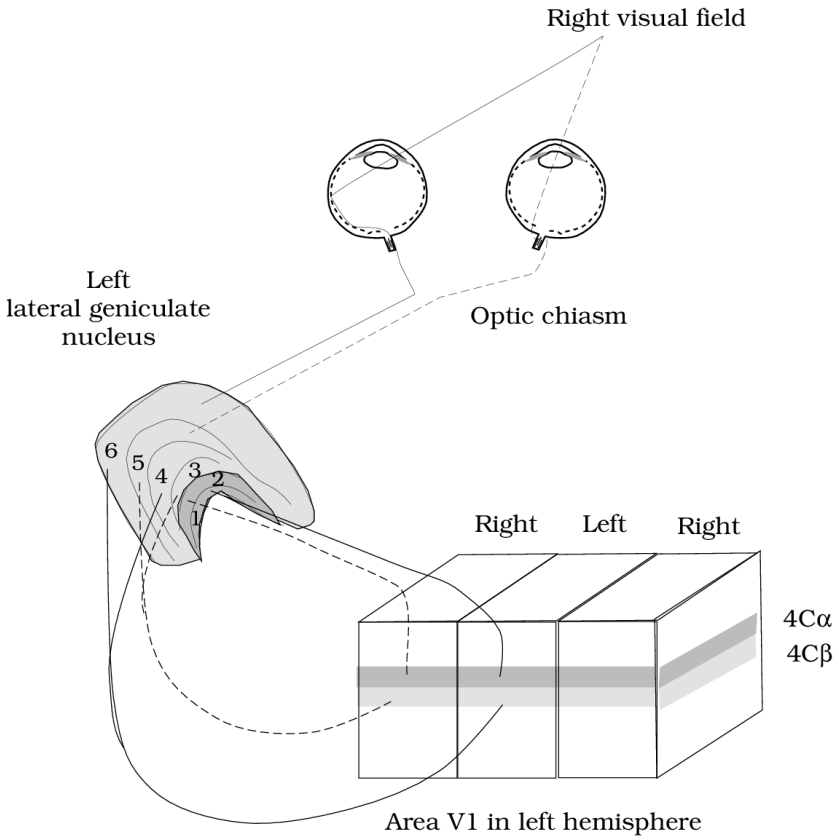

Figure 3.5.: Connections of the left LGN [27, p. 158].

As mentioned in section 3.2, different visual pathways origin from different types of ganglion cells in the retina. Signals from these midget and parasol cells are directed to specific layers in the LGN. This separation also persists in the primary visual cortex. Therefore, Layers 4Cα and 4Cβ are where the visual cortex receives signals from the LGN magnocellular and parvocellular layers, respectively.

The so called "retinotopic organization", which describes the relation between the ganglion cells spatial position in the retina and the location of corresponding neurons in the LGN, is preserved also in the visual cortex. This relation will be discussed in the following chapters and is also the main focus

of this master thesis (for an extensive review see [27].)

4. Retinotopic mapping of the primary visual cortex

For each voxel measured in the visual cortex there is a corresponding region of the visual field, a so-called receptive field. On the other hand every location in visual space is mapped onto a specific location of the visual cortex. This results in a retinotopic map. These maps have first been discovered by examining correlations of neurological war injuries and corresponding visual field losses [40].

This section will provide a brief overview on the development of retinotopic and receptive field mapping using functional magnetic resonance imaging. First I will discuss a paper published in 1994 by Engel et. al. [41], which illustrated the retinotopic behaviour of the primary visual cortex using BOLD fMRI for the first time. Subsequently I will present a paper published in 2008 by Dumoulin et. al. [1] where a new type of data analysis as well as stimulus were proposed.

4.1. fMRI of human visual cortex

In 1994 Engel et. al. [41] mapped the human visual cortex with BOLD-fMRI using an expanding ring stimulus. This stimulus consisted of a series of concentric rings which started as small dot in the center of the screen and slowly moved to the periphery by expanding their radius. As one ring vanished from the visual field, a new one emerged from the center. The expanding rings, which were constant in width, consisted of rapidly flickering black and white squares, while the background was gray (see figure 4.1).

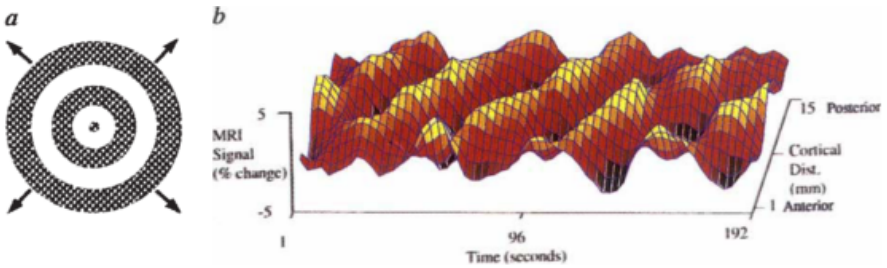

Figure 4.1.: (*a*) Illustration of the presented stimulus. An annulus containing a flickering checkerboard pattern was presented. Starting at the center, it then expanded to peripheral regions of the visual field. When the outer ring left the screen a new one spawned in the middle. This procedure was repeated four times during a 192 second long experiment. (*b*) The fMRI signal plotted as a function of time at each point within the calcarine sulcus. A temporal signal shift, which depends on the stimulus frequency, can be observed when moving from the posterior to the anterior sulcus. The central starting position of the stimulus is the reason for the shifts direction, as posterior regions are associated with the central visual field, while anterior regions correspond to peripheral regions [41].

Because of this retinotopic behaviour in the primary visual cortex, activity in the posterior calcarine sulcus corresponds to central ring stimuli, while the neural activation moves in the anterior direction as the rings reach a more peripheral location of the visual field. The stimuli therefore cause a traveling wave neural activation at each location of the calcarine sulcus (see figure 4.1).

4.2. Population receptive field estimates in human visual cortex

4.2.1. Stimuli

Using expanding ring stimuli (see section 4.1) the eccentricity corresponding to a specific voxel can be estimated, while so called "rotating wedges" (see figure 4.2) are used to measure the visual field angle. The rotating wedge stimulus consists of a 45° circle segment, which is slowly rotating. Similar to the expanding ring stimulus, the wedge contains a high contrast flickering dartboard pattern, while the rest of the circle is gray. Both stimuli are periodic and complete a full cycle in 24 seconds.

Conventional retinotopy experiments try to map a voxel on a single location

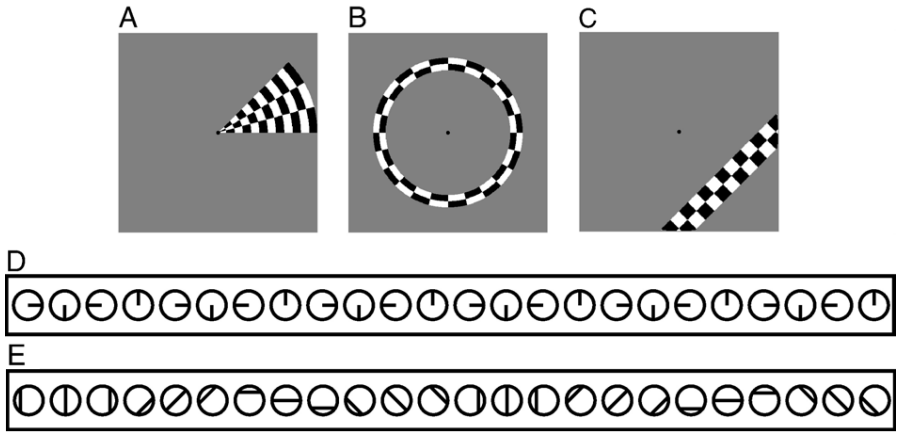

Figure 4.2.: Illustration of the stimuli. (A-C) Static images of the wedge, ring, and bar stimulus. D and E show the course of the wedge and bar stimuli during a single scan. D) The wedge rotates through 6 full cycles per scan. E) The bar moves through each of four orientations in two opposing directions during one scan [1].

of the visual field with the help of mentioned stimuli. The neural population located in a voxel however corresponds to a range of adjacent visual field locations which are also referred to as "population receptive field (pRF)" [42]. The method which is presented here builds on conventional techniques, but does not only estimate the most effective visual field location, but also the pRF size (Gaussian width parameter σ, see section 4.2.2) using responses from multiple stimuli [1]. Furthermore it allows the analysis of non-periodical stimuli, which is not possible using conventional traveling wave methods, because these methods use a sine of defined frequency to model the fMRI signal. Furthermore, analysis of non-periodical stimuli gives an estimate of the receptive field's size based on Cartesian coordinates rather than polar coordinates, which are used by ring and wedge stimuli.

An example for a non-periodic stimulus can be seen in Figure 4.2C. These drifting bars, which subtend one quarter of the total stimulus radius, move in a total of eight different directions during a single scan. Because there is no repetition of the stimulus, every visual field location, with the exception of the center, experiences a different, non-periodic excitation pattern.

4.2.2. Analysis

The MR-signal $y(t)$ can be described as

$$y(t) = p(t)\beta + e(t)$$

where $p(t)$ represents the prediction of the fMRI signal, β represents a scaling factor and $e(t)$ represents the error term.

It is now possible to estimate $p(t)$ using a appropriate function. In our case, a two-dimensional Gaussian pRF $g(x, y)$ is defined by three parameters; x_0, y_0 and σ and the following equation:

$$g(x, y) = e^{-\frac{(x-x_0)^2+(y-y_0)^2}{2\sigma^2}}$$

where (x_0,y_0) is the center and σ is the Gaussian spread (standard deviation).

Next, the effective stimulus $s(x, y, t)$ is defined. Because it is assumed that all parts of the stimuli contribute equally to the fMRI response[1] the formula describing the effective stimulus is simply a binary indicator function, which shows if the stimulus is present in a certain location at a given time or not.

Now, the pRF response is predicted for a given pRF model and effective stimulus, by calculating the overlap between the effective stimulus and the model pRF at a voxel:

$$r(t) = \sum_{x,y} s(x, y, t)g(x, y)$$

Subsequently $r(t)$ is convolved with a model of the hemodynamic response function $h(t)$[2], which was estimated separately for each subject:

$$p(t) = r(t) * h(t)$$

Finally the goodness-of-fit is estimated by computing the residual sum of squares (RSS) between the prediction, $p(t)$ and the data, $y(t)$, where β repre-

[1] fMRI responses to these kinds of stimuli are dominated by contrast edges and since the checkerboard revealing aperture (i.e. the ring, wedge and bar) is moving, contrast edges are present throughout the stimulated area. [43]

[2] See section 2.2.8

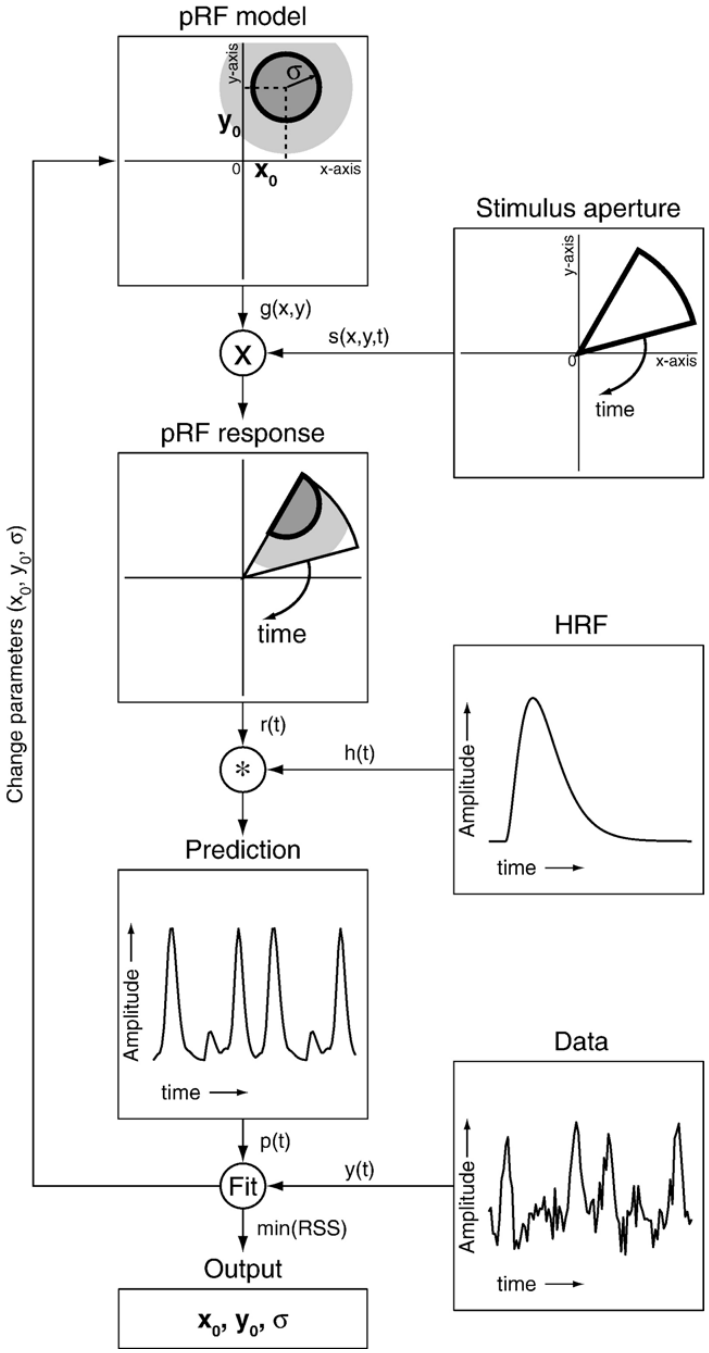

Figure 4.3.: Description of the pRF linear model estimation which is carried out for every voxel independently [1].

sents a scaling factor:

$$RSS = \sum_t (y(t) - p(t)\beta)^2$$

By minimizing the RSS, the optimal pRF parameters were found. Percent variance explained was used as primary measure of the goodness-of-fit.

This minimization was carried out in multiple steps. First, the functional data was resampled to an isotropic 1-mm resolution within the identified gray matter of the cortex and then smoothed along the cortical surface using a diffusion smoothing process[1] that approximated a 5-mm full-width at half maximum Gaussian kernel, which increased not only the signal-to-noise ratios by removing high spatial frequency noise, but also established a spatial correlation between voxels. Afterwards, 100,000 different fMRI time series predictions were created by changing the pRF model parameters ($x0$, $y0$ and σ) across a wide range of plausible values on a regular sampling grid. Because of the smoothing it is safe to only estimate the parameters on a smaller sample of the voxels (every other voxel) and accurately interpolate the other voxels, which greatly minimizes processing time.

In the second stage an optimization algorithm [45] to the 1-mm data was applied for every voxel whose first stage estimates explained more than 15% of the variance of the coarse fMRI signal. No smoothing was applied in this stage, as the final pRF size estimates are calculated by fitting data without any of the spatial smoothing used in the first stage. This coarse-to-fine approach is minimizing the processing time, while also increasing the likelihood of finding a global minimum and therefore a distinct result [1].

[1] Conventional Gaussian smoothing respects neither the nature of the tissue displayed in the image, nor the folded structure of the brain. In order to smooth only regions which strongly relate to each other in a sense of tissue type and geodesic distance, a new, surface oriented, type of smoothing has to be established. This method is based on the equivalence between Gaussian convolution and heat diffusion, which can be more easily adapted to a 2D lattice embedded in a three-dimensional space, and is therefore called "diffusion smoothing". For a detailed explanation see [44].

Part II.

Retinotopic Experiments

5. Traveling wave analysis

In order to describe periodic retinotopic stimuli a sinusoid of a frequency coinciding with the stimulus frequency, can be used (see figure 5.1).

To correctly estimate the corresponding receptive field for a given voxel in the visual cortex, the voxel's time course has to correlate strongly with the sinusoid. The challenge is now to find the best fitting sinusoid. It is possible to create a plethora of sinusoids in order to find the one which correlates the most. A different approach is to correlate only two sinusoid, namely the sinusoids corresponding to vertical and horizontal receptive fields (see figure 5.1b). Using the Statistic Parametric Mapping 8 (SPM8) software package developed at the Wellcome Trust Centre for Neuroimaging at University College London, sine and cosine regressors were created and estimated in a first-level analysis.

For a signal y, a general linear model (GLM) analysis

$$y(t) = \underline{X}\vec{\beta} + e(t)$$

estimates the parameter $\vec{\beta}$ for every voxel separately. $\underline{X}$ represents the design matrix consisting of the regressors, while $e(t)$ represents the error term. Multiple linear regression requires orthogonal regressors, which in our case are sine and cosine. Performing a GLM analysis we learn to which extend the signal is composed of our two sinusoids. Using sine and cosine regressors it is possible to describe the signal, because a phase shift of a sinusoid can be expressed as a combination of sines and cosines of a certain frequency.

By using the derived β terms, the phase ϕ of the ideal sinusoid can be calculated using the *arctan* function:

$$\phi = arctan\frac{\beta_{sine}}{\beta_{cosine}}$$

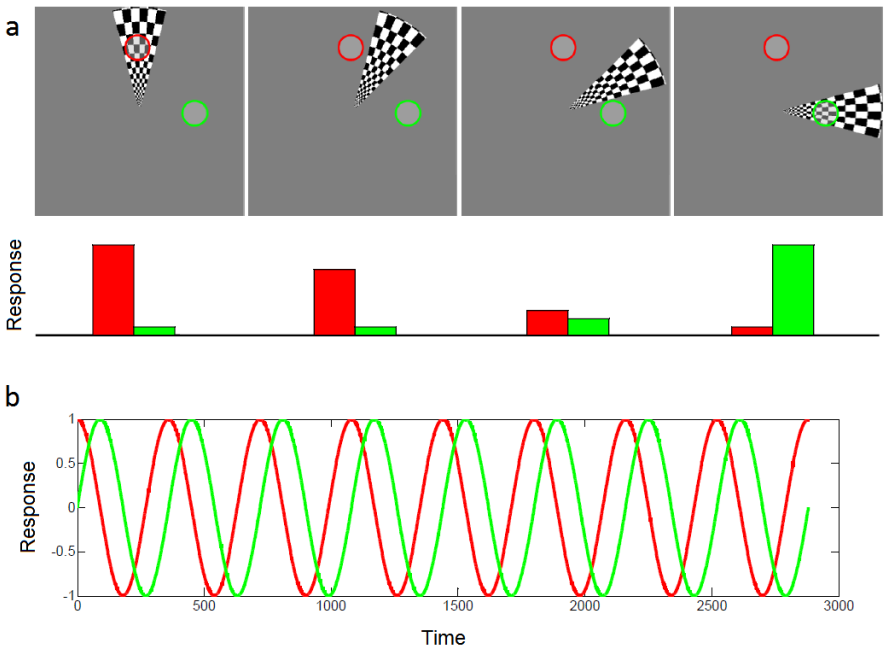

Figure 5.1.: a) Illustration of the induced response in a vertical and horizontal receptive field by a wedge stimulus b) The signal represents a traveling wave when observed over a given time. Adapted from [46].

and taking the sign of both arguments into account. This is done in order to return the appropriate quadrant of the computed angle in radians between the positive x-axis of a plane and the point (x,y)[1]. The result has a positive sign for counter-clockwise angles (y > 0) and a negative sign for clockwise angles (y < 0).

The amplitude $A(x,y)$ of a voxel at position (x,y) can be calculated by:

$$A(x,y) = \sqrt{\beta_{sine}(x,y)^2 + \beta_{cosine}(x,y)^2}$$

Hemodynamic lag correction

By performing the experiment twice, but having the stimulus move in opposite directions one can compensate for the hemodynamic lag[2].

If ϕ_{cw} represents the phase in the data when presenting a stimulus rotating clockwise and ϕ_{ccw} represents the phase when presenting a stimulus rotating counter-clockwise, the following applies:

$$\phi_{cw}(t) = \phi_s(t) + \phi_{hem}$$

$$\phi_{ccw}(t) = -\phi_s(t) + \phi_{hem}$$

ϕ_s is the phase associated with the stimulus, while ϕ_{hem} represents the constant phase shift induced by the hemodynamic lag. By subtracting both equations one can derive the "real" phase change, which only depends on the stimulus. In the following, we will refer to this method as "phase subtraction method".

There is also a second option to correct for the hemodynamic lag using the Fourier transform. Rather than calculating the phase and creating a new stimulus, the Fourier transform is calculated separately for each run, the imaginary component of one Fourier transform is inverted and the data sets are averaged back together. This is possible because the imaginary component of a Fourier transform represents the sine part, while the real component represents the

[1] This procedure is known as $atan2$ function in many computer languages.
[2] See section 2.2.8

cosine part. While inverting the even cosine part just changes the data as a mirrored stimulus would do, inverting the odd sine part simulates a stimulus moving in the opposite direction. After the inversion both datasets now origin from the "same" stimulus and thus averaging is possible. In the following, we will refer to this method as "Fourier combination method".

5.1. Traveling wave analysis of artificial data

5.1.1. Creation of an artificial volume

In order to verify the traveling wave analysis method a simulated data set was created. It consisted of 15x15x10 voxels and 180 volumes, which mimicked data acquired over the course of 180 seconds, i.e. TR = 1s[1]. The stimulus itself had a repetition time of 15s.

The volumes were split into two parts. Those sections, separated at the center of the x-axis, simulate measurements with stimuli moving in opposite directions. Voxels along the y-axis represent voxels located near each other, which show a retinotopic behaviour, i.e. show activation depending on the stimulus location. Because the stimulus period equals 15 seconds and the size of the y-dimension also equals 15, each voxel lights up consecutively for one second. Hence, a traveling wave arises. Additionally an artificial hemodynamic shift of three seconds was introduced. Variation along the z-axis consisted of linear increasing random noise. A signal intensity offset of 100 was introduced because of technical reasons, i.e. SPM data analysis.

Figures 5.2 and 5.3 illustrate the properties of the created volume.

As mentioned in section 5, two sinusoid regressors were built and SPM was used to estimate the model. Subsequently, the angle of the ideal sinusoid was calculated for every voxel using the two beta maps and the before mentioned $atan2$ function. Up to this point the sections of the artificial data which are based on stimuli moving in the opposite direction were processed separately.

[1]This means that the terms "second" and "volume" can be treated as synonyms in our example.

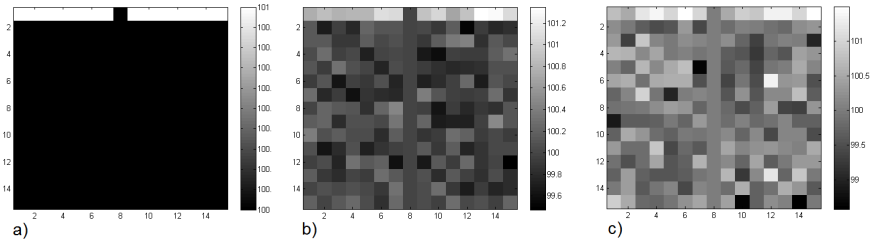

Figure 5.2.: Artificial volume without a hemodynamic shift. a) The first slice ($z = 1$) of the artificial volume at time $t = 0$. Activation due to the stimulus can be seen in white. b) Another slice ($z = 5$) of the volume at time $t = 0$. Moving up the slices we can see an increase in noise. c) The last slice ($z = 10$) of the artificial volume at time $t = 0$. Reaching the last slice a further increase of noise can be seen. The activation is now barely visible.

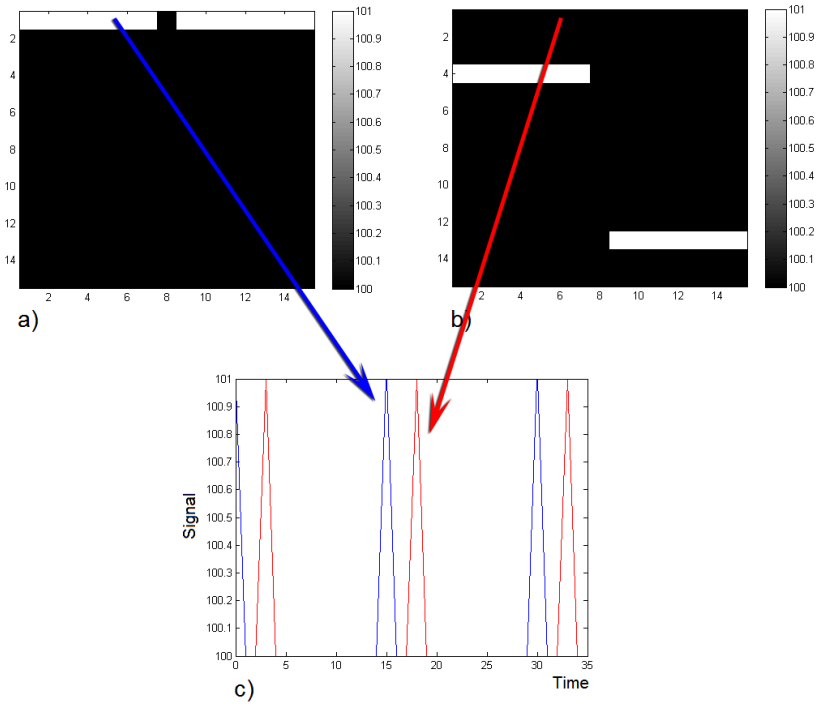

Figure 5.3.: a) The first slice ($z = 1$) of the artificial volume at time $t = 0$. b) The first slice ($z = 1$) of the artificial volume with a hemodynamic shift of 3 seconds at time $t = 0$. Due to the stimulus activating a certain voxel for the duration of exactly one second before moving on, the activation shifts from voxel 1 back to voxel 4 and 13 for the stimulus moving in the opposite direction, respectively. c) Illustration of the first three stimulus periods. The blue time course represents the voxel activated at time $t = 0$ (first row of image a)) without a hemodynamic shift. The red time course represents the same voxel, but with a hemodynamic shift of three seconds. Therefore, the voxel is now activated at time $t = 3$ for the first time.

5.1.2. Hemodynamic lag correction in the artificial volume

In order to correct for the hemodynamic delay we now apply the "phase subtraction method" (see section 5). By adding and subtracting the phases it is possible to calculate the "real" phase present in the signal.

In practice we are faced with problems due to periodicity of the stimulus and consequential folding. Figure 5.4 d) shows the "unfolded" phase data, which has been transformed to an interval ranging from $-\pi$ to π radiant. The adjacent voxel values, i.e. phase values, along the vertical axis differ from each other by $\frac{2\pi}{15}\,rad$, which is in agreement with the stimulus period of 15 seconds.

Additionally, the "Fourier combination method" (see 5) was applied to account for the hemodynamic delay. In contrast to the first method mentioned in section 5, we do not experience problems regarding phase "folding" here.

Comparison of the two methods

Figure 5.4 shows a comparison of the two methods, which hints at a higher signal to noise ratio when using the "phase subtraction method"[1].

To quantify the differences, the standard deviation of the noisy image slices compared to the reference slices $z = 1$ was calculated. The standard deviation was computed for each row along the vertical y-axis and subsequently averaged.

When using the Fourier transform to combine both runs and analyze them afterwards ("Fourier combination method"), the standard deviation values are about $0.72\,rad$ for $z = 5$ and $1.53\,rad$ for $z = 10$.

The mean standard deviation of the middle slice $z = 5$ equals about $0.11\,rad$ when both runs are processed separately and combined subsequently for hemodynamic lag correction ("phase subtraction method"). The standard deviation of the last slice $z = 10$ equals $1.21\,rad$. These results back up the impression of the "phase subtraction method" being superior.

[1] The vertical column between the two data sets only serves as visual separation and can be ignored. Because of different processing steps it possesses different values. For the "Fourier combination method" it represents a "NaN" values, whereas this "NaN" values have been converted to zeroes by SPM when performing the "phase subtraction method".

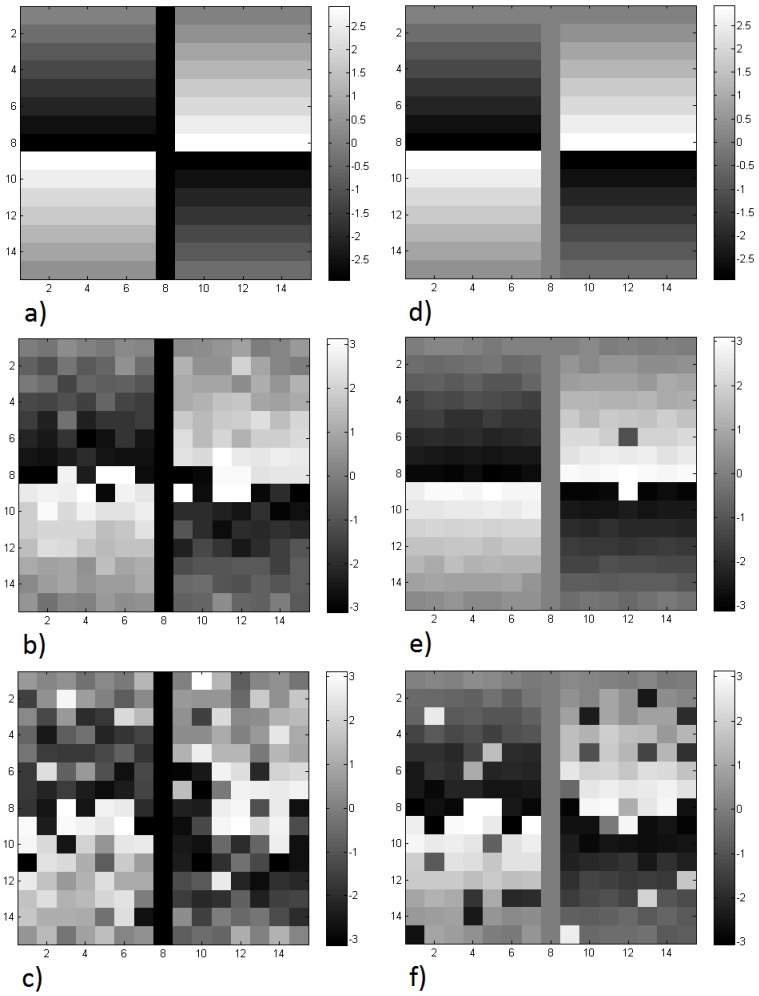

Figure 5.4.: Phase data transformed to the interval ranging from $-\pi$ to π radiant, which was created by analyzing artificial data with SPM using two sinusoid regressors. Image a,d) represent the first slice ($z = 1$) of the volume, while b,e) and c,f) show slices $z = 5$ and $z = 10$. Higher slice numbers correspond to higher noise which was added when building the volume. Data sets placed on the left and right of each image correspond to stimuli moving in the opposite direction. a-c) To correct for the hemodynamic delay both data sets were combined before SPM processing using "Fourier combination method". d-f) SPM estimated the data of each run separately. Subsequently the "phase subtraction method" was used. Especially high noise slices show better results if the phase subtraction method is used for hemodynamic lag removal.

5.2. Traveling wave analysis of acquired data

After verifying the traveling wave analysis method with the use of artificially produced data, "real" data from the scanner was processed.

5.2.1. Subject

One right-handed volunteer (male, 30 years) with normal visual acuity was measured.

5.2.2. Methods

Measurements

Scans were recorded on a SIEMENS Magnetom 7T scanner using a 32-channel head coil. Functional MR images of the visual cortex (TE/TR= 23/2000 ms, flip angle 70°) were acquired using an EPI sequence. There was no slice gap and the effective voxel size measured 1x1x1 m^3.

Additionally, an anatomical scan was conducted. A "mp2rage" sequence was used (TE/TR= 3.53/4500 ms, 0.7x0.7x0.7 mm^3, FOV = 31x38 cm^2), which shows homogeneous contrast due to the intrinsic correction of B1-inhomogeneities by combining two images measured at different inversion times. This procedure makes the T1-weighted images independent of proton density contrast [47].

Stimuli & Scans The visual stimulus was generated in the MATLAB (The MathWorks, Inc., Natick, MA) programming environment using the Cogent toolbox (Laboratory of Neurobiology, London). It consisted of a rotating double wedge, which measured about 1/5 of the screen with an opening angle of about 35° and an expanding ring, which covered half of the screen at maximum, i.e. when the whole ring was present. For a more detailed explanation of the stimuli see section 4.1 and 4.2.1.

It took the stimuli 30 seconds to complete one period, revealing a flickering checkerboard with a frequency of 8 Hz while doing so. This was repeated 12 times, resulting in a 6 minute long trial and 180 image volumes. During the

session a total of eight functional scans where conducted. The circle stimulus was presented rotating clockwise as well as counter-clockwise, while the ring was shown moving to the the center as well as moving in the direction of the periphery, respectively. Each of this four types of scans were repeated for improved specificity.

Before obtaining the final images, several preliminary steps have to be carried out on the raw data from the scanner. First, the data has to be "preprocessed", i.e. corrected for several common errors and artifacts.

Pre-Processing

Preprocessing of functional images was carried out using SPM8. In the following the applied preprocessing steps will be briefly described.

Slice-time correction Lying in the scanner, the subjects brain is not imaged at once, but one slice after another, which results in timing differences between imaging the first and the last slice. This means that each slice corresponds to a different point in time. Because a Fourier transform allows for a representation of any signal as a linear combination of sinusoids of different frequencies and phases, the routine adds a constant to the phase of every frequency, shifting the data in time in a such a way that it seems like the volume was imaged simultaneously as a whole. The necessity of this temporal correction was confirmed in recent studies [48].

Realignment It is possible that the quality of an fMRI run is strongly decreased by movement artifacts. Removing them is accomplished by realigning all scans to a so called reference scan. Mathematically this can be done by a least-squares approach, which minimizes intensity differences between image volumes.

Smoothing Spatial Smoothing was performed using a Gaussian filter with 2mm kernel width. Smoothing increases the signal-to-noise ratio of each voxel and lowers the number of "independent voxels". It is essential for obtaining

significant results, but the downside is a loss of spatial resolution, which is why finding an optimal level of smoothing for the used data is important. Because our aim is high spatial resolution, the smoothing kernel was kept small deliberately.

Segmentation

Introducing a segmentation step in data processing has multiple reasons. First, one can eliminate noise originating from white matter. Because white matter consists of myelinated nerve axons and glial cells, every active voxel found has to be a false-positive. Second, if the brain is properly segmented, i.e. the final segmentation does not contain any topological defects such as handles and cavities, it is possible to flatten the gray matter. By removing the strong convolutions of the brain, interrelations between the activated voxels can be easier identified.

Due to the nature of the mp2rage sequence, segmentation did not turn out to be trivial. While mp2rage delivers more homogeneous contrast when compared to conventional T1 imaging, there is excessive noise in regions outside of the brain (see figure 6.2). This property causes massive problems when using automatic segmentation software, which is essential for larger subject numbers. Nevertheless several pieces of software suited for image data analysis have been evaluated regarding automated mp2rage data segmentation.

SPM8 & SPM12 Using SPM8 no proper segmentation was possible. The same was true for SPM12 when it was given only the final mp2rage image. Performing multi-channel segmentation, i.e. using all acquired image volumes, with SPM12 the result could be notably enhanced. Nonetheless the quality of the data was not sufficient as it still had to be manually corrected for topological errors.

Caret Caret 5.65 (Van Essen Lab, St. Louis, Missouri) could not cope with the mp2rage data and only handle one hemisphere at a time. Due to frequent lockups no reasonable segmentation result could be obtained.

mrGray mrGray (Wandell Lab, Stanford, CA) provided much control over the segmentation process, as it was possible to set custom gray and white matter thresholds which's consequence were immediately shown in a preview. Unfortunatly, correction for topological defect had to be carried out manually once again.

itkGray The successor of mrGray, itkGray (Wandell Lab, Stanford, CA), only provided semi-automatic segmentation and was therefore unsuitable. Automatic work stages were possible, but their initial properties had to be defined manually.

Freesurfer Freesurfer 5.2.0 (Athinoula A. Martinos Center for Biomedical Imaging, Charlestown, Massachusetts) exited with an error, when receiving a mp2rage image volumes as input. Thus it was not possible to perform white and gray matter segmentation without manually interfering.

Additionally, brain extraction was performed prior to using the mentioned techniques. This attempt, as well as performing the segmentation on the mp2rage components (the image volumes which are used to calculate the final mp2rage image) were only partially successfull. Because no automatic segmentation was possible, SPM12 multi-channel segmentation was used and the data was corrected manually for topological errors with Caret 5.65.

5.2.3. Data Analysis

Further data analysis, i.e. the traveling wave analysis, was executed with the help of SPM8 and MATLAB 7.8. For details see section 5 and 5.1. In order to correct for the hemodynamic delay, the two runs with stimuli moving in opposite directions were combined after the analysis, as this method ("phase subtraction method") proofed itself as the superior one in terms of signal to noise ratio when applied onto artificial data (see section 5.1.2).

5.2.4. Results

Figure 5.5 shows the results of both, the rotating wedge and the expanding ring experiment. The activation maps are overlaid on the flattened cortex using Caret. The retinotopy of the visual cortex, explained in section 4.1, can be clearly seen in form of adjacent semicircles for the expanding ring stimulus and wedges for the rotating wedge stimulus, respectively.

As the circles represent the stimulus eccentricity and the wedges represent its polar angle, it is possible to map a region of V1 onto the visual field using polar coordinates.

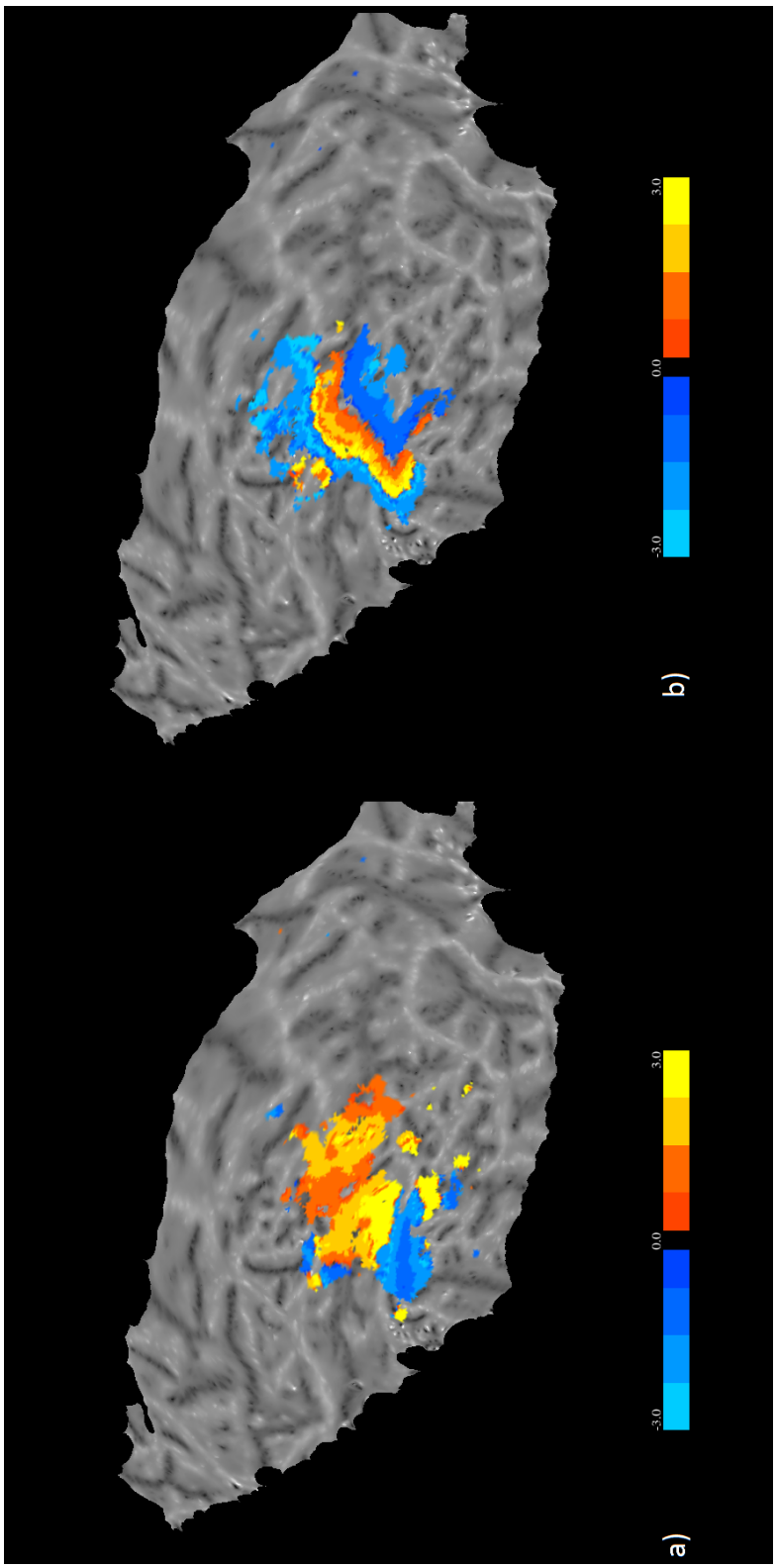

Figure 5.5: Right occipital cortex flattened with Caret. The phase values of the functional images range from $-\pi$ to π and are thresholded at a t-value of 15. a) Overlay of activation evoked by the rotating wedge stimulus. b) Overlay of activation evoked by the expanding ring stimulus.

6. Population receptive field estimates using mrVista

Recently a new method for pRF mapping was introduced by Dumoulin et. al. (see section 4.2). As this approach allows for a more accurate retinotopic mapping, i.e. mapping not only the pRF location, but also its spread, additional data has been recorded and evaluated using this very procedure. The functional data was obtained using a multiband EPI sequence, which enabled higher resolution imaging when compared to conventional sequences.

In order to test for the reliability of our approach we also simulated localized central and peripheral vision loss.

6.1. Subject

One right-handed volunteer (male, 24 years) with normal visual acuity was measured. Because both eyes send visual signals to both hemispheres, his left eye was covered to eliminate superimposed activation. By reducing this factor of variance, we hope to improve the results reproducibility.

6.2. Methods

6.2.1. Measurements

Scans were recorded on a SIEMENS Trio 3T scanner using a 32-channel head coil. Functional MR images of the visual cortex (TE/TR= 42/1000 ms, flip angle 60°) were acquired using a CMRR multiband EPI sequence (multiband

acceleration factor = 3) [22]. The slice gap of the 39 recorded slices was 1.15 mm and the effective voxel size measured 1.5 x 1.5 x 1 m^3. A total of 192 time frames were acquired per run.

Additionally an anatomical scan composed of 160 slices was conducted using a "mprage" sequence (TE/TR= 4.21/2300 ms, 1 x 1 x 1.1 mm^3).

6.2.2. Stimuli & Scans

At first, the visual stimulus was generated in the MATLAB (The MathWorks, Inc., Natick, MA) programming environment using the Cogent toolbox (Laboratory of Neurobiology, London). It consisted of a moving bar, which measured 1/5 of the screens width. After 18 seconds, the bar crossed the screen once, revealing a flickering checkerboard with a frequency of 8 Hz while doing so. Subsequently the bar rotated 45° clockwise and changed its moving direction. Therefore, it took the stimulus 144 seconds to cross the screen in 8 different directions before reaching its initial state and terminating (see figure 6.1 and also section 4.2.1).

In order to simplify data processing, the stimulus was then replicated using the "vistadisp" toolkit from "mrVista" (Wandell lab, Stanford, CA). This enabled seamless transfer from the stimulus presentation parameters to the pRF estimation software. The new stimulus had a slightly longer period of 192 seconds.

During the session a total of five functional scans where conducted. In order to improve specificity, the mean of these runs was used for pRF-estimation.

In addition to regular stimulation, central and peripheral vision loss was simulated. This was achieved by covering a certain region of the visual field permanently with the background color and therefore stimulating only in the central and peripheral visual field, respectively.

Figure 6.1 shows the stimuli associated with the three different experiments.

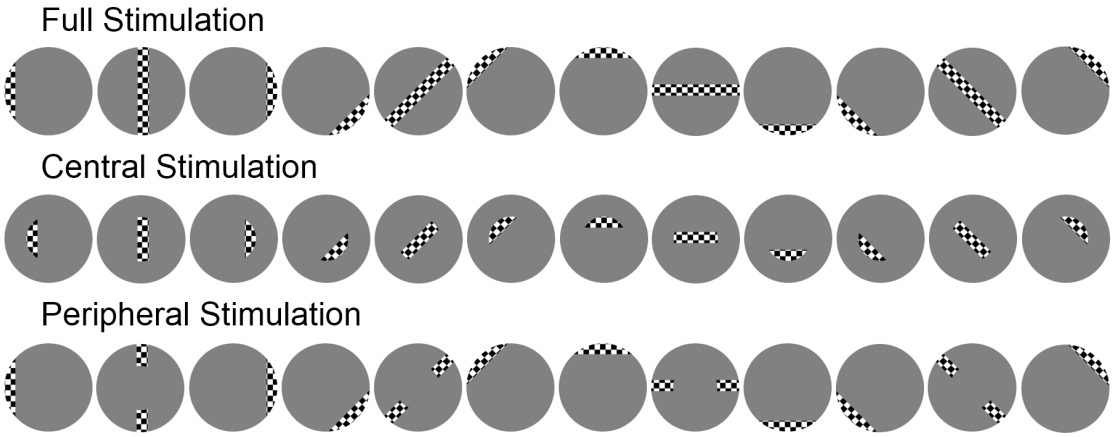

Figure 6.1.: Illustration of the first half of the presented stimuli. After crossing the screen from bottom left to top right, the bar turns 45° clockwise again and continues to cross the screen four times (see also figure 4.2). The presented stimuli had either no simulated vision loss, simulated peripheral vision loss or simulated central vision loss of 5°.

6.2.3. Pre-Processing

Because of the used multiband EPI sequence, which records multiple slices at once, conventional slice-time correction is not applicable and was therefore not conducted.

Realignment and smoothing with a 2mm Gaussian kernel with SPM8 was carried out similar to the pre-processing of the rotating wedge and expanding ring data described in section 5.2.2.

6.2.4. Segmentation

Recapitulating section 5.2.2, no (proper) automatic segmentation was possible using any of the evaluated software. As already mentioned in section 6.2.1, we therefore decided to switch to a more common anatomical sequence called "mprage" in order to avoid tedious manual segmentation of the brain. This move provides us with with working automatic processing using Freesurfer at the cost of a reduced signal to noise ratio and longer processing time. Nevertheless automatic segmentation, which requires little to no manual corrections outweighs the cons in this case.

In figure 6.2 the results of automated mp2rage and mprage segmentation

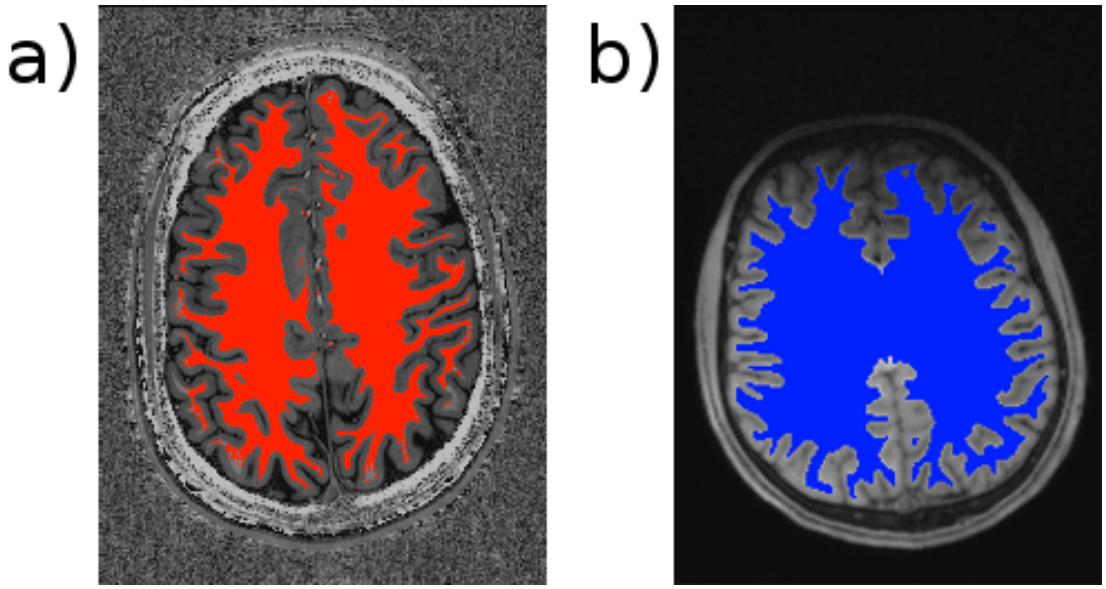

Figure 6.2.: a) Sample slice of an image segmented with SPM12, which was recorded using a mp2rage sequence at 7T. Due to the apparent errors like cavities, manual error correction is necessary. One can also see the noise outside of the head, which leads to automatic segmentation being so difficult for images created by mp2rage sequences. b) Sample slice, which shows the result of an automatic segmentation using Freesurfer. The displayed image was recorded using a mprage sequence at 3T. The high contrast of the brain and skull compared to the background makes it easier to process, i.e. segment these images. The resulting automatic segmentation requires very little to no manual correction.

using SPM12 and Freesurfer, respectively, are visualized.

6.3. Data Analysis

Data analysis was executed with mrVista using a population receptive field estimation model implemented in Matlab 7.8. Subsequently, the BOLD response of each voxel was predicted using a two-dimensional Gaussian pRF model, which estimated the center location and spread of the most responsive voxel positions. The ideal pRF parameters for each voxel then were then identified by minimizing the residual sum of squares between the predicted and observed fMRI time series.

For a more detailed explanation of the analysis see section 4.2.2.

The analysis of the data corresponding to the stimuli with simulated lo-

calized vision loss was identical to the standard procedure, i.e. the analysis program was told that a standard eight-bar stimulation had been performed.

6.4. Results

It can be seen in figure 6.3, that the pRF analysis showed the expected posterior to anterior increase of the eccentricity parameter in area V1. The occipital pole therefore corresponds to visual stimuli presented at the center of the visual field, which is illustrated by hot colors. Likewise, anterior regions correspond to stimulation of the more peripheral regions, which is illustrated by cold colors.

Figure 6.4 displays the flattened visual cortex of both hemispheres. The transition from voxels corresponding to central regions, to voxels corresponding to peripheral ones is also very visible on the overlaid eccentricity maps.

The phase angle overlay shows abrupt changes of the angle value i.e. reversals of the polar angle representation. This regions can be understood as boundaries, which can be used to classify different regions of the visual cortex. [49]

The images were thresholded with a coherence threshold of 0.2 to make sure that the voxels had adequate coherence with the fitted pRF model.

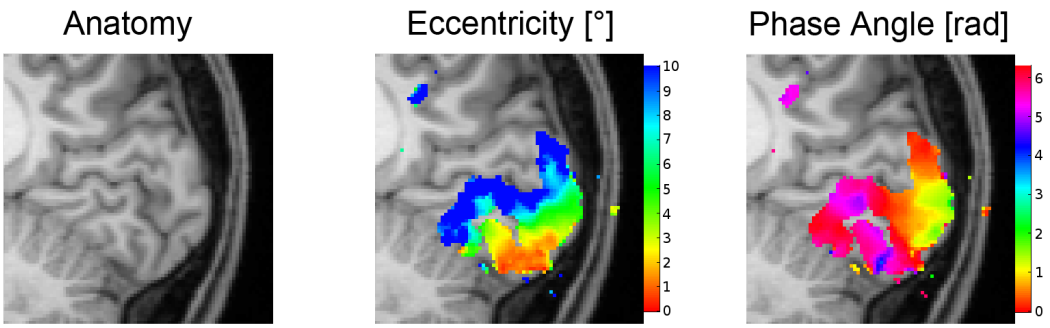

Figure 6.3.: Additional to a sagittal MPR image of the occipital lobe for guidance, the pRF analysis results of a full stimulation are displayed. They show the expected posterior to anterior increase of the eccentricity parameter. Looking at the representation of the phase angle one can clearly see distinct areas and clear borders of the different areas representing certain polar angles.

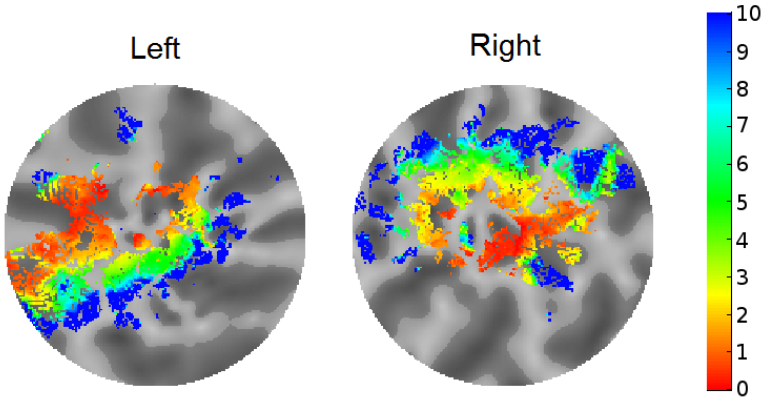

Figure 6.4.: Flattened visual cortex overlaid with eccentricity activation maps of the eight-bar experiment and threshold at a coherence threshold 0.2.

6.4.1. Simulated localized vision loss

Examining figure 6.5 one can see that a localized vision loss indeed causes a loss of activation in the voxels, which were associated with the affected visual field locations by the full stimulation experiment. By analyzing the data in the same way we did when using a full stimulus, we confirm the relations of the voxels located in V1 and positions in the visual field.

Figure 6.6 further illustrates the results of the pRF analysis by visualizing the estimated pRF centers on the visual field. The vision deficits agree with the vision loss induced by the stimuli, which can be seen more clearly by increasing the coherence threshold to 0.4.

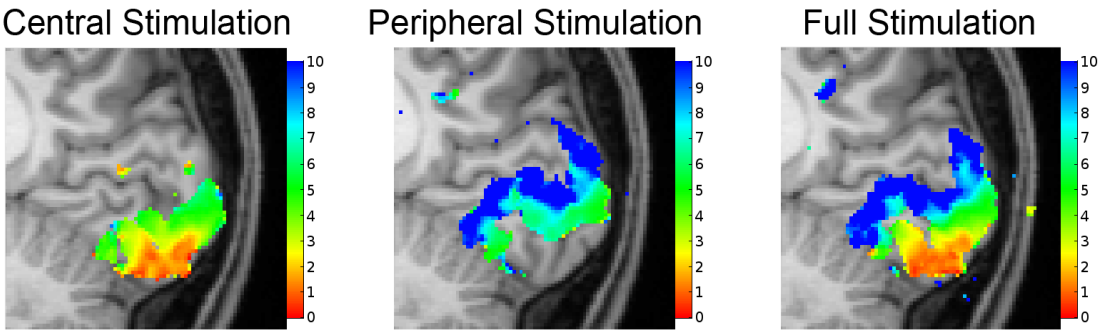

Figure 6.5.: Eccentricity activation maps evoked by a stimulus with simulated peripheral vision loss, simulated central vision loss and no simulated vision loss. It is apparent that the first two images are subsets of the final one.

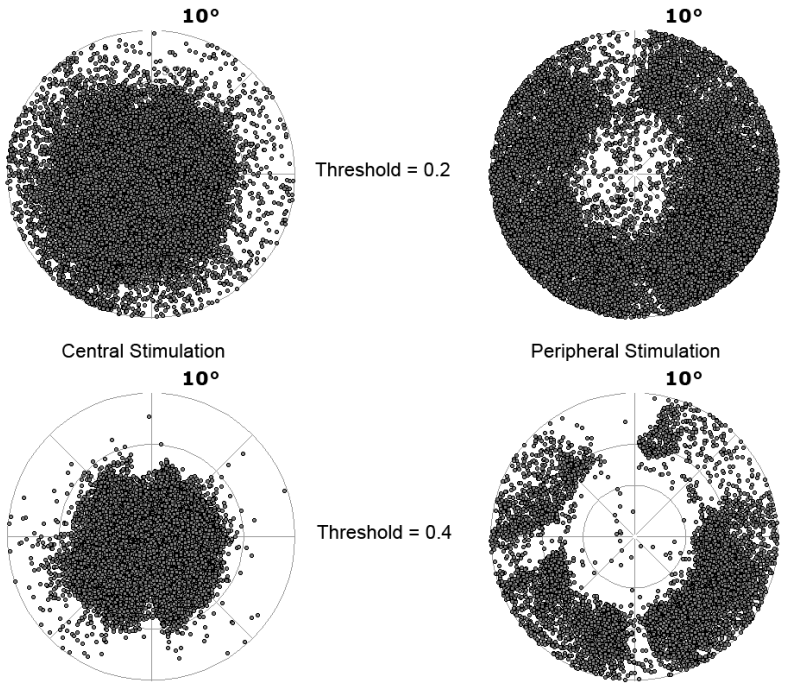

Figure 6.6.: Estimated pRF centers plotted on the visual field.

6.5. Discussion

Our findings are in agreement with previously published studies [1,41], while featuring high-resolution multiband imaging allowing for more precise mapping.

Furthermore it was shown that detection of localized vision loss is possible with the applied method.

Accurate pRF mapping, which is achieved using this technique could be of particular importance for studies in patients suffering from localized loss of vision in the visual field as shown in [50]. In this paper the possibility of reorganization, i.e. remapping of the primary visual cortex is assessed. In order to examine these remapping processes patients suffering from age-related macular degeneration and Stargardt disease were examined using similar stimuli as used in this chapter.

Nevertheless, future studies are required to assess reproducibility and enhance sensitivity of pRF maps across repeated functional runs. Custom surface coils, which allow for a higher SNR when compared to regular head coils, could also be used to increase the spatial resolution of occipital lobe imaging considerably. This is achieved by only imaging the part of the brain, the surface coil rests on, i.e. narrowing the field of view.

7. Conlusion and Outlook

Retinotopic mapping can be used to functionally map regions of the primary visual cortex V1 to the corresponding positions of the visual field. Within the context of this master thesis different methods for retinotopic mapping have been discussed. A traveling wave analysis method was successfully verified using artificially created data and then applied to an acquired fMRI data set. The resulting activiation maps were visualized by using an underlay of flattened gray matter. The phase values of the rotating wedge and expanding ring stimulus yielded maps corresponding to the polar angle and eccentricity of the stimulus, respectively. It is therefore possible to map a region of V1 onto the visual field using polar coordinates.

In order to improve the quality of the retinotopic mapping another technique was introduced. In contrary to periodic wedge and ring stimuli an eight-bar stimulus was used. Population receptive field modeling made it possible to analyze this non-periodic stimulus by estimating a visual field position in cartesian coordiates, as well as spread for each voxel above threshold in the primary visual cortex.

Both approaches yielded results in agreement with previously published studies [1,41].

Mapping was verified by introducing artificial stimulus dropouts. This showed that central and peripheral stimulation indeed only activate voxels which correspond, according to regular retinotopic mapping, to central and peripheral visual field regions, respectively.

With the help of the presented retinotopy methods, diseases like age-related macular degeneration (AMD) can be understood in more detail. In a paper by Baseler et. al. [50] for example, the ability of V1 to remap itself in case of AMD was investigated using pRF modeling.

Other disorders like glaucoma, where peripheral vision is affected, could also be examined using retinotopic mapping. However, due to the narrow opening of the scanner, stimulation of peripheral regions provide a challenge.

To further improve the quality of retinotopic mapping custom surface coils, which allow for a higher resolution and SNR when compared to regular head coils, can be used. Figure 7.1 displays such a custom 7 channel surface coil built in our lab, while figure 7.2 shows the results, i.e. eccentricity maps, of an eight-bar experiment (for data analysis methods see chapter 6) performed with this very coil. One can see the strong signal gradient of the anatomical measurement, as well as the reduced FOV of the functional scan. Applying this coils in combination with multiband sequences, the number of slices covering the occipital lobe could be multiplied, when compared to traditional retinotopic mapping.

Figure 7.1.: Photograph of the custom 7 channel surface coil built in our lab.

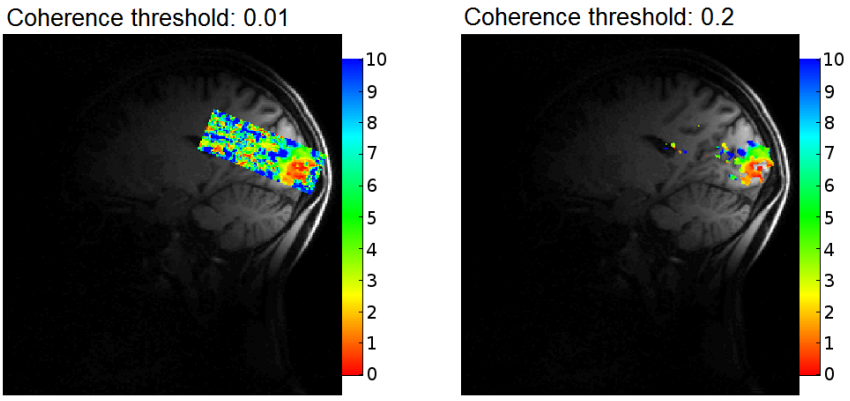

Figure 7.2.: Eccentricity maps of an eight-bar experiment. On the left, the reduced functional scan FOV of the custom surface coil is illustrated by choosing a very low coherence threshold. The image on the right-hand side shows that by increasing the threshold, the anticipated eccentricity maps are indeed achieved.

Bibliography

[1] S O Dumoulin and B A Wandell. Population receptive field estimates in human visual cortex. *Neuroimage*, 39(2):647–660, 2008.

[2] I I Rabi, J R Zacharias, S Millman, and P Kusch. A new method of measuring nuclear magnetic moment. *Physical Review*, 53(4):318, 1938.

[3] Torrey Purcell H. Pound. Resonance absorption by nuclear magnetic moments in a solid. *Physical Review*, 69(1-2):37–38, 1945.

[4] F Bloch, W W Hansen, and M Packard. Nuclear Induction. *Physical Review*, 69(3-4):127, 1946.

[5] Hansen Bloch F. Methods and means for chemical analysis by nuclear inductions., 1951.

[6] S Meiboom and D Gill. Modified Spin-Echo Method for Measuring Nuclear Relaxation Times. *Review of Scientific Instruments*, 29(8):688–691, 1958.

[7] Purcell H Carr. Effects of diffusion on free precession in nuclear magnetic resonance experiments. *Physical Review*, 94:630–638, 1954.

[8] E L Hahn. Spin Echoes. *Physical Review*, 80(4):580–594, 1950.

[9] R Damadian, K Zaner, D Hor, and T Dimaio. Human Tumors Detected by Nuclear Magnetic-Resonance. *Proc Natl Acad Sci U S A*, 71(4):1471–1473, 1974.

[10] P C Lauterbur. Image Formation by Induced Local Interactions - Examples Employing Nuclear Magnetic-Resonance. *Nature*, 242(5394):190–191, 1973.

[11] Ernst R. Gyromagnetic resonance fourier transform zeugmatography., 1978.

[12] W A Edelstein, J M Hutchison, G Johnson, and T Redpath. Spin warp NMR imaging and applications to human whole-body imaging. *Phys Med Biol*, 25(4):751–756, 1980.

[13] L Sokoloff, M Reivich, C Kennedy, M H Des Rosiers, C S Patlak, K D Pettigrew, O Sakurada, and M Shinohara. The [14C]deoxyglucose method for the measurement of local cerebral glucose utilization: theory, procedure, and normal values in the conscious and anesthetized albino rat. *J Neurochem*, 28(5):897–916, 1977.

[14] M Reivich, D Kuhl, A Wolf, J Greenberg, M Phelps, T Ido, V Casella, J Fowler, E Hoffman, A Alavi, P Som, and L Sokoloff. The [18F]fluorodeoxyglucose method for the measurement of local cerebral glucose utilization in man. *Circ Res*, 44(1):127–137, 1979.

[15] S Ogawa, T M Lee, A R Kay, and D W Tank. Brain magnetic resonance imaging with contrast dependent on blood oxygenation. *Proc Natl Acad Sci U S A*, 87(24):9868–9872, 1990.

[16] Committee on Data for Science and Technology. `http://physics.nist.gov/cgi-bin/cuu/Value?gammap`.

[17] Malcolm H Levitt. *Spin Dynamics: Basics of Nuclear Magnetic Resonance*. John Wiley & Sons, 2008.

[18] F. Schmitt, M.K. Stehling, and R. Turner. *Echo-Planar Imaging*. Springer-Verlag Berlin Heidelberg, 1998.

[19] Frank Schneider and Gereon R Fink. *Funktionelle MRT in Psychiatrie und Neurologie*. Springer, 2007.

[20] Http://www.medical.siemens.com/. `http://www.medical.siemens.com/siemens/en_GLOBAL/gg_mr_FBAs/files/apps/MAGNETOM_world/MR_Manuals/MR_Basics/USA_English/Magnets_Spins_and_`

Resonances/Magnets_Spins_and_Resonances/Advanced/Content/MagnetsSpinsResonances/contrasts_1.htm.

[21] M Blaimer, F Breuer, M Mueller, R M Heidemann, M A Griswold, and P M Jakob. SMASH, SENSE, PILS, GRAPPA: how to choose the optimal method. *Top Magn Reson Imaging*, 15(4):223–236, 2004.

[22] S Moeller, E Yacoub, C A Olman, E Auerbach, J Strupp, N Harel, and K Ugurbil. Multiband multislice GE-EPI at 7 tesla, with 16-fold acceleration using partial parallel imaging with application to high spatial and temporal whole-brain fMRI. *Magn Reson Med*, 63(5):1144–1153, 2010.

[23] P T Fox and M E Raichle. Focal physiological uncoupling of cerebral blood flow and oxidative metabolism during somatosensory stimulation in human subjects. *Proceedings of the National Academy of Sciences of the United States of America*, 83(4):1140–4, February 1986.

[24] P T Fox, M E Raichle, M A Mintun, and C Dence. Nonoxidative glucose consumption during focal physiologic neural activity. *Science (New York, N.Y.)*, 241(4864):462–4, July 1988.

[25] Nikos K Logothetis. The neural basis of the blood-oxygen-level-dependent functional magnetic resonance imaging signal. *Philosophical transactions of the Royal Society of London. Series B, Biological sciences*, 357(1424):1003–37, August 2002.

[26] G K Aguirre, E Zarahn, and M D'esposito. The variability of human, BOLD hemodynamic responses. *NeuroImage*, 8(4):360–9, November 1998.

[27] Brian A Wandell. *Foundations of Vision*. Sinauer Associates, Inc., 1995.

[28] National Eye Institute. http://www.familyconnect.org/parentsite.asp?SectionID%20=99&TopicID=371&DocumentID=3840.

[29] Drenckhahn D (Hrsg) Benninghoff A. Zenker W. (Hrsg). *Anatomie*, volume 2. Urban und Schwarzenberg, 1993.

[30] Michael Schünke Adolf Faller Gabriele Schünke. *Der Körper des Menschen.* Georg Thieme Verlag, 15 edition, 2008.

[31] R G Foster. Neurobiology: bright blue times. *Nature*, 433(7027):698–699, 2005.

[32] D A Baylor. Photoreceptor signals and vision. Proctor lecture. *Invest Ophthalmol Vis Sci*, 28(1):34–49, 1987.

[33] D M Dacey and B B Lee. The 'blue-on' opponent pathway in primate retina originates from a distinct bistratified ganglion cell type. *Nature*, 367(6465):731–735, 1994.

[34] W H Merigan, L M Katz, and J H Maunsell. The effects of parvocellular lateral geniculate lesions on the acuity and contrast sensitivity of macaque monkeys. *The Journal of neuroscience : the official journal of the Society for Neuroscience*, 11(4):994–1001, April 1991.

[35] D Fitzpatrick, K Itoh, and I T Diamond. The laminar organization of the lateral geniculate body and the striate cortex in the squirrel monkey (Saimiri sciureus). *J Neurosci*, 3(4):673–702, 1983.

[36] J S Lund, R D Lund, A E Hendrickson, A H Bunt, and A F Fuchs. The origin of efferent pathways from the primary visual cortex, area 17, of the macaque monkey as shown by retrograde transport of horseradish peroxidase. *J Comp Neurol*, 164(3):287–303, 1975.

[37] D H Hubel and T N Wiesel. Ferrier lecture. Functional architecture of macaque monkey visual cortex. *Proc R Soc Lond B Biol Sci*, 198(1130):1–59, 1977.

[38] D L Adams, L C Sincich, and J C Horton. Complete pattern of ocular dominance columns in human primary visual cortex. *J Neurosci*, 27(39):10391–10403, 2007.

[39] D H Hubel and T N Wiesel. Binocular interaction in striate cortex of kittens reared with artificial squint. *J Neurophysiol*, 28(6):1041–1059, 1965.

[40] R S Fishman. Gordon Holmes, the cortical retina, and the wounds of war. The seventh Charles B. Snyder Lecture. *Documenta ophthalmologica. Advances in ophthalmology*, 93(1-2):9–28, January 1997.

[41] S A Engel, D E Rumelhart, B A Wandell, A T Lee, G H Glover, E J Chichilnisky, and M N Shadlen. fMRI of human visual cortex. *Nature*, 369(6481):525, June 1994.

[42] J D Victor, K Purpura, E Katz, and B Mao. Population encoding of spatial frequency, orientation, and color in macaque V1. *Journal of neurophysiology*, 72(5):2151–66, November 1994.

[43] S A Engel, G H Glover, and B A Wandell. Retinotopic organization in human visual cortex and the spatial precision of functional MRI. *Cerebral cortex (New York, N.Y. : 1991)*, 7(2):181–92, March 1997.

[44] A Andrade, F Kherif, J F Mangin, K J Worsley, A L Paradis, O Simon, S Dehaene, D Le Bihan, and J B Poline. Detection of fMRI activation using cortical surface mapping. *Human brain mapping*, 12(2):79–93, March 2001.

[45] R. Fletcher and M. J. D. Powell. A Rapidly Convergent Descent Method for Minimization. *The Computer Journal*, 6(2):163–168, August 1963.

[46] UCL Institute of Cognitive Neuroscience. `http://www.icn.ucl.ac.uk/courses/MATLAB-Tutorials/Session2010-2011/Retinotopy.pdf`.

[47] José P Marques, Tobias Kober, Gunnar Krueger, Wietske van der Zwaag, Pierre-François Van de Moortele, and Rolf Gruetter. MP2RAGE, a self bias-field corrected sequence for improved segmentation and T1-mapping at high field. *NeuroImage*, 49(2):1271–81, January 2010.

[48] Ronald Sladky, Karl J Friston, Jasmin Tröstl, Ross Cunnington, Ewald Moser, and Christian Windischberger. Slice-timing effects and their correction in functional MRI. *NeuroImage*, 58(2):588–94, September 2011.

[49] Jonas Larsson and David J Heeger. Two retinotopic visual areas in human lateral occipital cortex. *The Journal of neuroscience : the official journal of the Society for Neuroscience*, 26(51):13128–42, December 2006.

[50] Heidi A Baseler, André Gouws, Koen V Haak, Christopher Racey, Michael D Crossland, Adnan Tufail, Gary S Rubin, Frans W Cornelissen, and Antony B Morland. Large-scale remapping of visual cortex is absent in adult humans with macular degeneration. *Nature neuroscience*, 14(5):649–55, May 2011.

List of Figures

Danksagung

Bedanken möchte ich mich bei Professor Ewald Moser, Leiter der Arbeitsgruppe am Exzellenzzentrum.

Außerdem möchte ich speziellen Dank an meine Betreuer Professor Christian Windischberger und Professor Gerald Badurek richten. Dank ihnen konnte ich diese Arbeit verfassen.

Mein Dank gilt auch meinen Kollegen Ronald Sladky, Martin Küblböck, André Hoffman, Roland Boubela, Martin Tik, Lucia Navarro de Lara und Jürgen Sieg, welche mich durch etliche Anregungen und Diskussionen während der Entstehung dieser Arbeit unterstützten.

Speziell möchte ich mich auch bei Professor Serge Dumoulin (Utrecht University) und Professor Michael Hoffmann (Universität Magdeburg) bedanken. Sie ermöglichten mir etliche Probleme zu lösen und Unklarheiten zu beseitigen.

Bedanken möchte ich mich auch bei meinen Eltern und meiner Freundin Suhal, welche mir immer motivierend zur Seite standen.